# PLASMONIC METASURFACES AND DYNAMIC BEAM-STEERING AT TERAHERTZ FREQUENCIES

by

James Hirst

A thesis submitted to the faculty of
The University of Utah
in partial fulfillment of the requirements for the degree of

Master of Science

Department of Electrical and Computer Engineering

The University of Utah

August 2015

**The University of Utah Graduate School**

# STATEMENT OF THESIS APPROVAL

The thesis of **James Hirst**

has been approved by the following supervisory committee members:

| | | |
|---|---|---|
| **Berardi Sensale-Rodriguez** | , Chair | **04/20/2015** Date Approved |
| **David Schurig** | , Member | **04/20/2015** Date Approved |
| **Jeffrey Walling** | , Member | **04/20/2015** Date Approved |
| **Michael Scarpulla** | , Member | **04/20/2015** Date Approved |

and by **Gianluca Lazzi**, Chair/Dean of

the Department/College/School of **Electrical and Computer Engineering**

and by David B. Kieda, Dean of The Graduate School.

## ABSTRACT

To dynamically arbitrarily shape electromagnetic wavefronts has always presented a challenge in millimeter wave and terahertz (THz) technologies. While traditional optical components such as lenses and mirrors can provide the ability to do so, a common issue that might present a problem for long-term technologies is how to dynamically steer a beam without employing mechanical parts. However, recent developments in terms of metamaterial technologies and new materials, such as liquid crystals and phase changing materials, show that it may be possible to create devices that can dynamically steer a beam using little-to-no mechanical parts. Static devices of this nature have already been created by others for the near-infrared region. However, few of such devices exist in the THz region, where demonstrations of dynamic beam steering are scarce. The purpose of this thesis is to explore dynamic beam steering of THz waves using metasurfaces from numerical simulations, which will be correlated with results from a preliminary test device that has been fabricated and measured.

This thesis will contain an overview of a metamaterial device designed and fabricated to steer a THz beam. It will first review the mathematics and physics behind such a design. Then simulations used to design the device will be discussed. Finally, this thesis will describe the experimental procedures used to test the prototype structures, and discuss the results.

This work is dedicated to my wonderful parents, Bud and Kathy, who encouraged, supported, and inspired me throughout the entirety of my school career; my girlfriend, Antonia Knoblich, who has been a friend, inspiration, and mentor through thick and thin; and finally, to my brother and sister, Sam and Alex, whom I hope I have inspired for the better.

**TABLE OF CONTENTS**

## LIST OF TABLES

## LIST OF FIGURES

## ACKNOWLEDGEMENTS

I would like to thank my thesis advisor, Prof. Berardi Sensale-Rodriguez, for his mentorship and guidance with this research. I discovered this wonderful area of research in optoelectronics and THz technologies through him and he made this thesis and many other things possible for me.

I am grateful to Prof. Ashutosh Tiwari and his research group for providing $VO_2$ samples with which to fabricate and test the devices researched in this project.

I thank Prof. David Schurig for his continued guidance, for extensively teaching me about both analytical and simulated calculations done for this thesis, and for being in my thesis committee. I would also like to thank Prof. David Schurig for his class that taught me to use commercial computational electrodynamic software necessary to perform simulations on the devices used for these experiments.

I thank Prof. Mike Scarpulla and his research group for allowing us to borrow and use equipment necessary for performing the experiments. I would also like to thank Prof. Mike Scarpulla for being on my thesis committee and for his class that taught me how to use the nanofabrication lab, which was necessary for fabricating the devices used in these experiments.

I thank Prof. Jeffrey Walling for his guidance in my research as well as his class that taught me to use the CAD tools necessary to design the devices used in the experiments.

I would like to thank my colleague, Sara Arezoomandan, who has worked with and guided me tirelessly throughout the entirety of this project and helped fabricate the designs as well as provide me experimental results. This project would not have been possible without her unending guidance and support of me.

Lastly and certainly not least, I would like to thank both Andrew Paulsen and Prof. Nahata. Andrew's hard work and Prof. Nahata's equipment made the experimental parts of Chapter 3 possible, provided numerous resources for their methods of fabrication and measurements, and provided me with physical results for the devices in this thesis.

# CHAPTER 1

# INTRODUCTION

Metamaterials are a very recent development in physics and engineering that enable us to shape electromagnetic radiation in ways that would be impossible with any normal material found in nature. This past decade alone has seen hundreds if not thousands of new advancements in metamaterials and their applications. These advancements are currently giving us unprecedented control over the electromagnetic forces found both in natural and artificial settings [1] [2] [6].

## 1.1 Introduction to Metamaterials

The refractive index is a property of matter that is dependent of the energy of an electromagnetic wave interacting with it and which therefore affects the electromagnetic wave propagation. It describes how light interacts with electric fields and is determined by the atomic structure of a material. However, metamaterials are able to display unusual electromagnetic properties due to periodic subwavelength features in their structure. For instance, one property that does not exist in nature but can be achieved through metamaterials is that of a negative index of refraction [1].

Another important formulation and observation developed from the theoretical study of metamaterials is that it is possible to redirect electromagnetic fields with a

metasurface by designing it in such a way where the conserved fields such as the electric displacement field, the magnetic induction field, and the pointing vector are displaced consistently [2]. The field of "transformation optics" generalizes this approach of controlling electromagnetic radiation through steady phase changes accumulated along an optical path. The next sections will review the mathematic and physical properties of light in depth from a transformation optics perspective and will motivate the work reported in this thesis.

### 1.2 Fermat's Principle and Generalized Laws of Reflection and Refraction

Huygens' Principle states that the wave-fronts created from a point source of light are spherical waves centered at the point source. In time, each point on the wave-front becomes a source of secondary wavelets and a new wave-front is built up from the accumulation of these wavelets. For a continuous source, the process repeats [3]. This principle explains the change in direction of a wave-front upon entering a different material interface.

Fermat's principle dictates that a narrow beam of light will go through the path of least transit time when propagating between two points A and B:

$$Optical\ Path = \int_A^B n(\vec{r})dr \tag{1.1}$$

Equation 1.1 defines the optical path where $n(\vec{r})$ is the local index of refraction.

Fermat's principle for light can be illustrated by Feynman's drowning man dilemma, which is depicted in Figure 1.1, and where a wall with varying height is inserted along the seashore. If the wall does not exist, since the lifeguard runs faster on land than he swims in the sea, there is an optimal path the lifeguard could potentially take

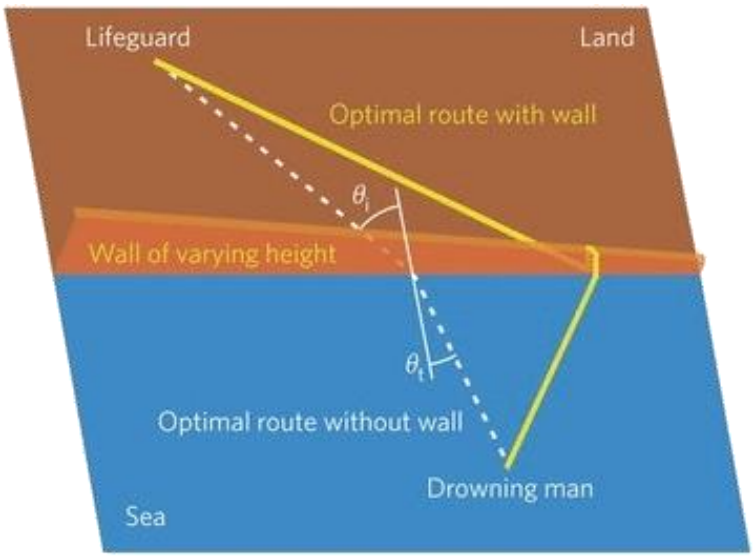


Figure 1.1 Drowning Man's Dilemma with Wall of Varying Height. Reprinted by permission from Macmillan Publishers Ltd: Nature Materials [4], copyright 2014. The white dashed path shows the optimal lifeguard path without the wall of varying height. The solid yellow line shows the optimal lifeguard path when a wall of varying height is inserted along the seashore.

represented by a white-dashed line in Figure 1.1. However, since the wall height increases from right-to-left, this path might not be optimal when introducing the wall. The optimal path in this case shifts.

In general, the optimal route satisfies:

$$\frac{sin\theta_i}{v_{land}} - \frac{sin\theta_t}{v_{water}} = 0 \tag{1.2}$$

where $v_{land}$ and $v_{water}$ are the lifeguard speeds on land and water, respectively. This is the same form as Snell's law:

$$\frac{sin\theta_i}{v_i} - \frac{sin\theta_t}{v_t} = 0 \tag{1.3}$$

where $v_i$ and $v_t$ are, respectively, the phase velocities of light before and after the light

goes through an optical interface [5].

The wall of varying height comes into play, optically-wise, when a constant gradient of phase-shift is inserted at the interface. In the drowning man's dilemma, the optimal route takes the least amount of time with respect to the other routes. Likewise, an optical path in the presence of phase gradients will take the least amount of time and energy possible in the total accumulated optical phase [6] [7]. Figure 1.2 shows the schematic used with this principle in order to derive a generalized law of reflection and refraction [8]:

$$\sin(\theta_t)\, n_t - \sin(\theta_i)\, n_i = \frac{\lambda_o}{2\pi}\frac{d\Phi}{dx} \tag{1.4}$$

This implies that if one is able to locally control the phase gradient, the refracted beam can be steered in any direction given that a suitable constant phase discontinuity $\frac{\mathrm{d}\Phi}{\mathrm{dx}}$ is constructed along the interface. This phase gradient gives the electromagnetic wave two angles of refraction, two critical angles, and two angles of reflection: one group of which are the "traditional angles" and the other group being the anomalous angles obtained from the generalized Snell's law.

Figure 1.2 contains the same lines as Figure 1.1. It shows the actual geometric schematic used to derive the generalized Snell's law. The blue and red lines represent two different paths for the light while Φ and Φ + dΦ are phase shifts when the paths cross the boundary. In order to solve for the Generalized Snell's law, one must utilize Calculus of Variations in addition to the schematic to derive the formula in equation 1.4. The assumption made is that the interface between the two media is artificially designed in such a way that introduces the desired phase discontinuity to produce the anomalous refraction phenomena.

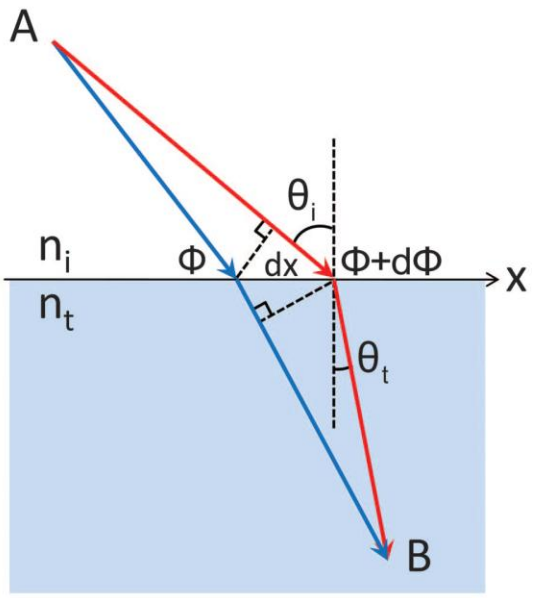


Figure 1.2 Schematics Used to Derive the Generalized Snell's Law. An incident electromagnetic wave propagates from the top ($n_i$) into the bottom one ($n_t$), $\theta_i$ is the incidence angle. From [8]. Reprinted with permission from AAAS.

### 1.3 Nanoantenna Arrays

One possible way to steer a beam utilizing metasurfaces is by designing an adequate resonator array on top of a dielectric substrate. This array of resonators can work well as a reconfigurable phase gradient due to the locally introduced phase shifts between the emitted and incident radiation at resonance and the subwavelength nature of each unit cell. By tailoring the geometry of the resonator array, one can build an arbitrary phase profile along the air/substrate interface. Phase shifts from the individual resonators need to cover a difference from 0° to 360° to provide full control of the electromagnetic wave propagation.

Previous works have shown that one can introduce phase discontinuities for an incoming wave front using V-shaped resonators; the phase shift in this case is a function of the arm dimensions, the angle between the arms, and the spatial alignment [8] [9].

The phase gradient, $\frac{d\Phi}{dx}$ in this case, is essentially an additional momentum contribution that is introduced by coupling to the nanoantennas and breaking the symmetry at the interface. Figure 1.3 shows each of the antennas scattering a y-polarized incident field. The red slope indicates that, when observing along the x-axis, the electric field is scattered at a difference of 1 μm from its neighbors which corresponds to a π/4 phase difference for the 8 μm incident plane wave meaning the phase shifts are clearly present for the cross-polarized light. This is the basis for the derivation and resulting design of many different devices bending light in ways that would not ordinarily be found in nature.

### 1.4 The THz gap

The THz frequency range falls between the microwave and far infrared range in the frequency spectrum. Historically, this range of frequencies has been called "the THz

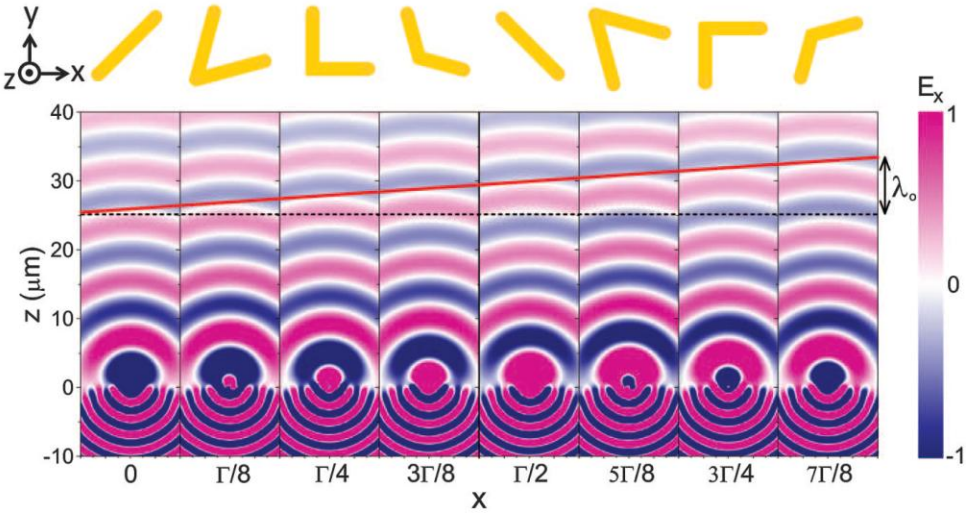


Figure 1.3 FDTD Simulations of Scattered Electric Field for Individual Nanoantennas. From [8]. Reprinted with permission from AAAS.

gap" due to the lack of practical technologies either operating at these frequencies or capable of interacting with waves of these frequencies. Figure 1.4 shows where the THz gap is located with respect to other areas of the electromagnetic spectrum [20].

THz electromagnetic waves have low energy while being nonionizing thus biological tissue can be safely exposed to it without fear of damage [20]. THz waves are electromagnetically susceptible to metals and can be reflected by them [20]. These attributes makes their use compelling for chemical, biomedical, and security imaging technologies [20].

One of the more attractive aspects of THz technology is that it can be used in astronomy applications [21]. The THz gap contains roughly half of the total luminosity of the Universe and 98% of photons emitted since the Big Bang so it is essential to develop technologies capable of detecting THz energies if we want to better understand the origins of the Universe [11]. Recent technologies have made great advances in detecting THz photons from outer space [12].

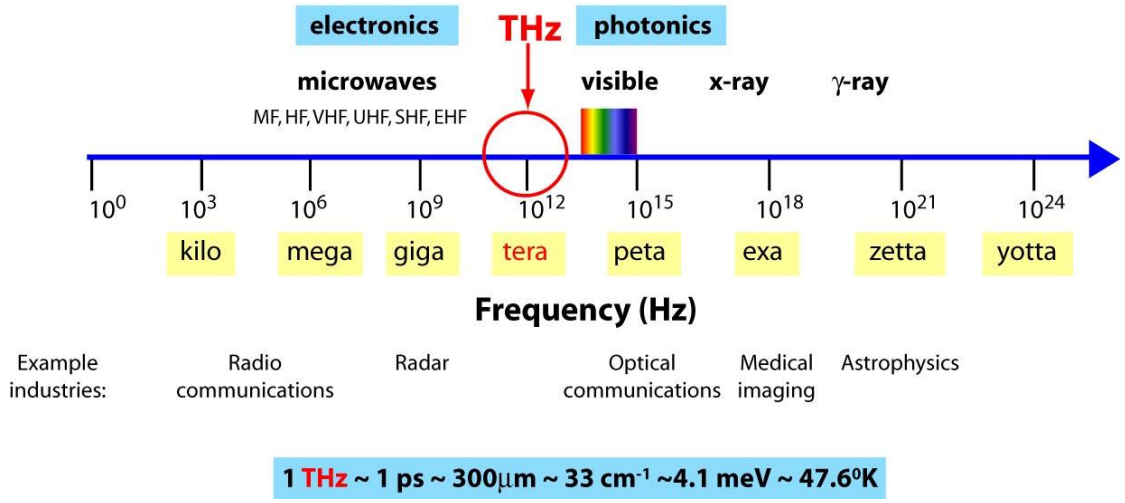


Figure 1.4 Frequency Spectrum Regions [10]. doi:10.1088/0034-4885/69/2/R01 

One issue faced by THz antennas is that, in order to couple between a receiving and emitting in THz waves, i.e. with frequency greater than or equal to 300 GHz, the maximum size for an omnidirectional antenna is roughly around 250 μm because of the maximum efficiency of an antenna being when designed at a quarter-wavelength. Trying to enhance the THz antenna collection in any way due to its small dimensions results in an increase in directivity meaning that radiation is more biased towards one direction and has to be aimed at the receiver. In other words, enhancing the antenna to increase its collection results in the antenna losing its omnidirectional properties. This is illustrated in Figure 1.5.

There is therefore a need to create THz smart antenna arrays that are capable of overcoming these tradeoffs. While technically it would not be possible to create a fully-omnidirectional antenna with a meaningful collecting area, the previous section has shown that it is possible to steer a beam in a way that could be directed in the direction of the receiver without mechanically changing the orientation of the beam via employing metasurfaces.

More importantly, the V-antenna metasurfaces from previous work [8] can be scaled in size to operate at other frequencies. The previous works have used this design at much higher frequencies than the THz, such as the near infrared.

The linear scalability of the metasurface allows one to utilize the same design for lower frequencies by scaling the device to larger proportions. Using a nonreconfigurable material, such as metal as previous authors did [8], gives a fixed functionality in bending the wave-front. In order to perform controlled beam-steering. However, it is possible to use a material whose electromagnetic properties can be tuned.

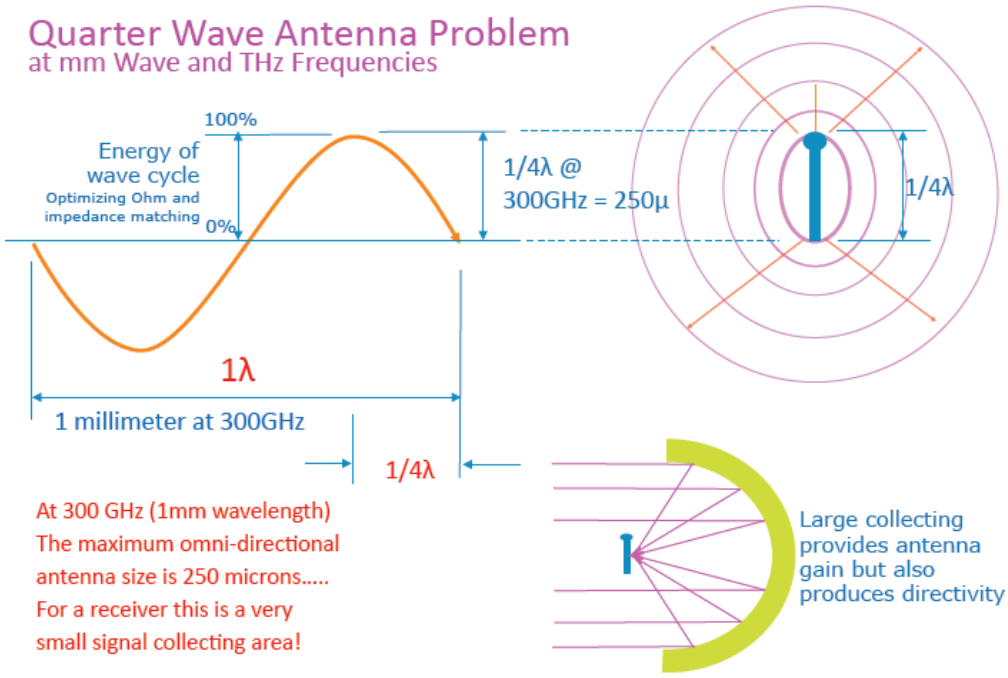


Figure 1.5 Dynamic Beam Steering Is Needed to Establish Link.

## 1.5 Phase-Transition Materials

Phase-transitioning materials are condensed matter materials, such as an insulator or semiconductor, which undergo a drastic change in their electrical or optical properties upon an environment change. One type of phase transition material is such that undergoes a metal-insulator transition.

The type of metal-insulator transitions are divided into groups of “structural” or “electronic” depending upon the mechanism of the transition. A structural transition occurs when a change in a material’s crystal lattice splits the electron conduction band.

Figure 1.6 demonstrates an example of a structural phase change in $TiO_2$ with an anatase mineral structure. Resistance measurements reveal an increase of 40% in conductivity of pressure-treated Nb-doped $TiO_2$ in comparison to the perfect anatase phase.

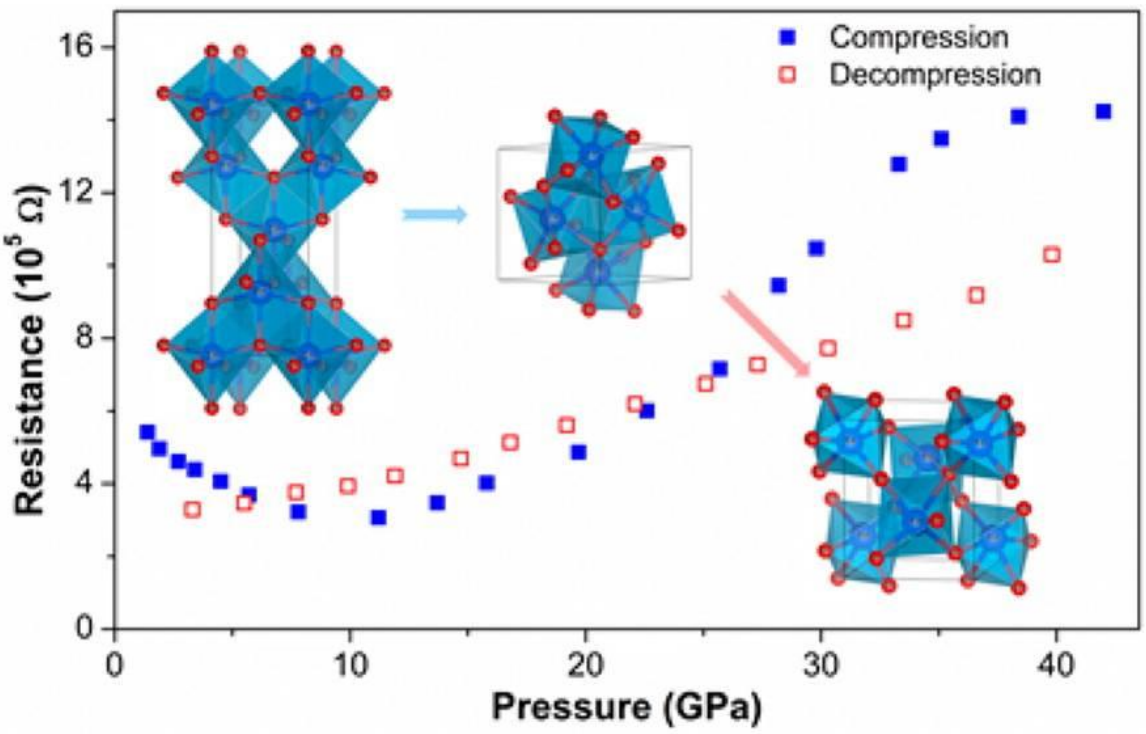


Figure 1.6 Anatase $TiO_2$ Structural Phase Transition Due to Pressure. Reprinted (adapted) with permission from Journal of The American Chemical Society [18]. Copyright 2014 American Chemical Society.

An electronic transition can be described by models in which the structure lattice is fixed: a material with sufficiently small lattice spacing will have a high electron density causing electric fields to be damped when imposed upon the ion cores of the structure meaning the material is in a metallic state. For lattice spacing larger than a critical value of the material, the damping will cease and the material will undergo a phase transition to an insulator. The criterion for this electronic transition is given by [13] [14]:

$$(n_c)^{\frac{1}{3}}\alpha_H \cong 0.25 \tag{1.5}$$

where $n_c$ is the critical volumetric electron density and $\alpha_H$ is the Bohr radius.

We wish to use a kind of phase-transitioning material that does not require direct Newtonian force to reduce the need for mechanical parts for our proposed device.

### 1.5.1 Vanadium Dioxide ($VO_2$)

Vanadium dioxide is a unique phase-transitioning material. It has a reversible phase transformation property where it changes from a semiconductor with monoclinic crystal symmetry to a metallic state with a tetragonal rutile structure which can be triggered by temperature, electric field, or laser excitation.

The exact mechanism of the phase transition for $VO_2$ is unknown and is the source of much debate [29]. The most common explanation is that both the lattice and Coulomb repulsion contribute to the insulator-to-metal transition [30]. The numerous results in previous works do verify that regardless of the mechanism, the transition from an insulator to a metal occurs when the material is heated past 68° C. Figure 1.7 (a) shows a vanadium dioxide lattice structure when it is in its insulator phase. Figure 1.7 (b)

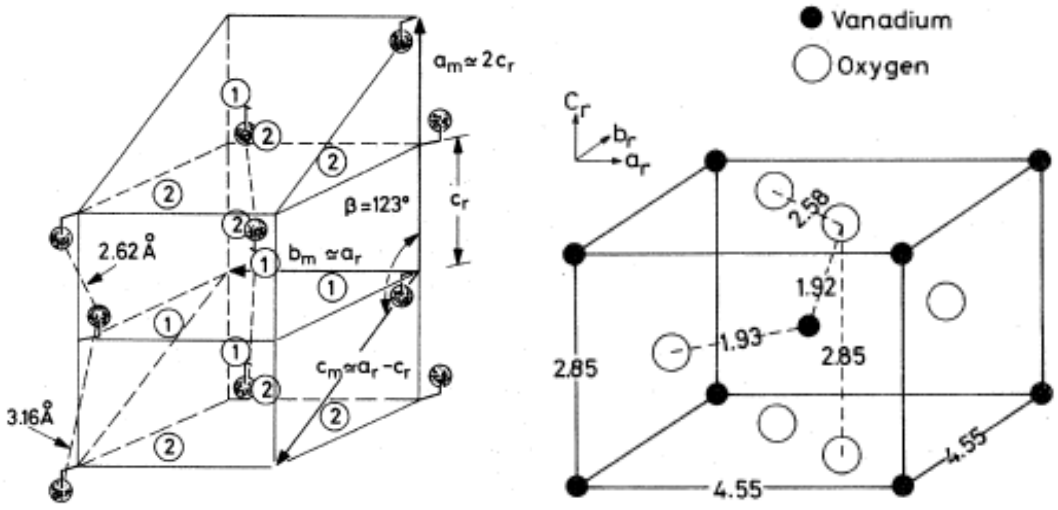


(a) (b)

Figure 1.7 $VO_2$ Structure in Insulator Phase (a) and $VO_2$ Structure in Metallic Phase (b). Reprinted (figure) with copyright permission from [15]. Copyright 1975 by the American Physical Society.

shows a vanadium dioxide lattice structure after transitioning to the metallic phase. The lattice has a distorted rutile structure before transitioning and has a tetragonal rutile structure after the phase transition takes place.

The $VO_2$ films experimentally investigated in this work, in order to show the feasibility of the proposed dynamic beam steering mechanism, consisted of a ~100 nm thick layer deposited over ~500 µm thick c-sapphire sapphire substrates. The deposition was carried out using a pulsed laser technique. A dense commercially-available $V_2O_5$ target was ablated using a Lambda Physik KrF excimer laser (pulse of 25 ns, λ=248 nm) for 10,000 pulses at a repetition rate of 10 Hz. During the deposition the substrate temperature was held at 600 °C while 9.7 mTorr of oxygen flowed. The crystallinity and phase purity of the $VO_2$ was confirmed using X-ray diffraction. Figure 1.8 illustrates the THz Spectrometer setup used to test the $VO_2$ samples. The phase transition of the films was tested by heating them by putting the films on a hot plate. The heated films were then

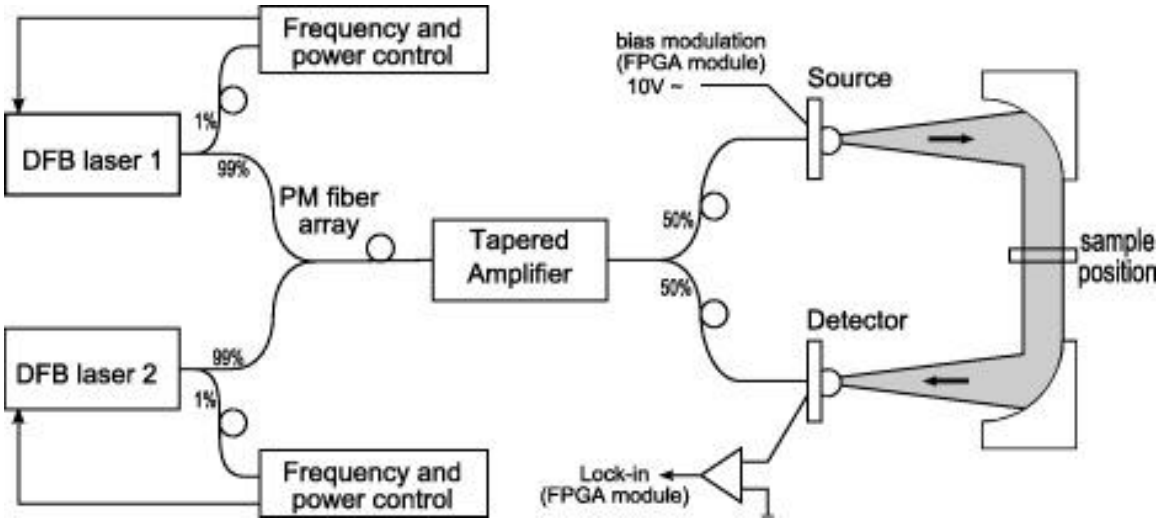


Figure 1.8 $VO_2$ Sample Testing Setup [38]. doi:10.1088/1367-2630/12/4/043017. © IOP Publishing & Deutsche Physikalische Gesellschaft. CC BY-NC-SA

quickly analyzed using a Toptica Photonics THz Spectroscopic Analyzer. The transmission through a device in the spectroscopic analyzer can be determined by the magnitude of the detected photocurrent. The magnitude of transmittance is inversely proportional to the conductivity of the material as a higher conductivity means more absorption/reflection of a device. If the photocurrent through the detector is large in magnitude, it means that the conductivity of the sample is low enough that the electromagnetic waves are able to go through the sample more easily. The tests performed on the fabricated samples resulted in two of the samples exhibiting phase transition properties when heated. The photocurrent is then recorded as a function of time for an optical frequency of 500 GHz. The sample is put on a hot plate set to 300° C for several minutes before taking the sample and placing it in the optical path.

Two of our $VO_2$ samples exhibited the desired phase transition after heating them for several minutes on the hot plate. The data were recorded on a laptop connected to the spectrometer setup.

Figures 1.9 (a) and (b) both show that each of the two samples exhibits a high level of electrical conductivity, which is represented by a low detected photocurrent, and then transitions back to an insulation phase, i.e. large photocurrent, when cooled down.

The conductivity of the sample can be extracted from the transmittance using the following formula [31-33] [37].

$$\frac{T}{T_0} = \left| \frac{1}{1 + \frac{Z_0 \sigma}{(1 + n_{sub})}} \right|^2 \tag{1.5}$$

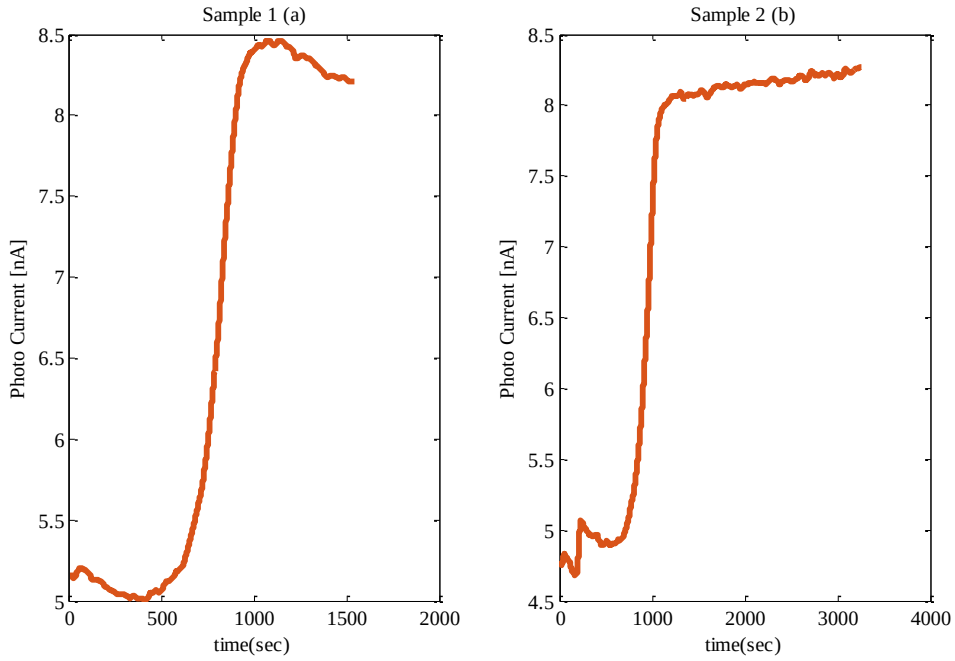


Figure 1.9 The Transmission Results of $VO_2$ Sample 1 (a) and Sample 2 (b).

where $T$ and $T_0$ are the transmittance of the sample when heated and the transmittance of the sample when cooled, respectively, and $n_{sub}$ is the refractive index of the sapphire substrate.

Equation 1.5 can be rewritten to extract the conductivity:

$$\sigma = \frac{\left(\sqrt{\frac{T_0}{T}} - 1\right)(n_{sub} + 1)}{Z_0} \tag{1.6}$$

The photocurrent levels when the sample is in metallic state correspond to conductivity levels of 405.5 ($\Omega^{-1}cm^{-1}$) and 426.5 ($\Omega^{-1}cm^{-1}$), respectively. These values are in excellent agreement with references [34], [35], and [36]. Now that we can confirm the properties of our $VO_2$ sample work as desired, we can further explain our motivation.

## 1.6 Motivation

In section 1.1, we introduced metamaterials and their capabilities for manipulating electromagnetic waves in ways not found in nature. In section 1.2, we introduced and described the derivation of the generalized laws of reflection and refraction. Moreover, section 1.3 introduced a type of metamaterial surface that can be used to exploit the generalized laws of reflection and refraction to steer a beam in an arbitrary direction. Section 1.4 introduced the THz gap and the need for the ability to steer THz beams to establish links between emitting and receiving antennas in the THz range. And finally, section 1.5 introduced and described phase-changing materials and the properties of $VO_2$. Section 1.5 also described our experiments with $VO_2$ and demonstrated its phase transition.

Combining the knowledge acquired from each of these sections, we propose a device that exploits the generalized laws of reflection and refraction in order to steer a THz beam. This work discusses numerical simulation of such a device and correlates these numerical results with experimental results of passive samples fabricated and tested at the University of Utah. The device will consist of $VO_2$ as the material for the V-shaped antennas on top of an insulator substrate so that the beam can be dynamically steered, as shown in simulations, by exploiting the material phase transition in $VO_2$.

# CHAPTER 2

## DESIGNING A DEVICE

Due to the fact that the devices we investigate are made of different materials and target different wavlengths than those reported in Ref. [8], we needed to be able to calculate the expected response of the devices via employing numerical simulations. This allows for optimization of the design based on variations in the dimensional and material properties.

Calculating the properties of the device in a simulated environment requires solutions to Maxwell's equations.

$$\nabla \times \boldsymbol{E} = \frac{\partial \boldsymbol{B}}{\partial t} \tag{2.1a}$$

$$\nabla \times \boldsymbol{H} = \boldsymbol{J} + \frac{\partial \boldsymbol{D}}{\partial t} \tag{2.1b}$$

$$\nabla \cdot \boldsymbol{D} = \rho \tag{2.1c}$$

$$\nabla \cdot \boldsymbol{B} = 0 \tag{2.1d}$$

Maxwell's equations (2.1a-d) are partial differential equations that describe all classical electromagnetic wave phenomena [17]. They are not analytical and require numerical methods to be solved. There are many methods and software that accompany these methods to solve Maxwell's equations. Among the most common methods are the Finite Element Method (FEM), the Finite Difference Time-Domain method (FDTD), and

the Method of Moments (MOM).

This chapter aims to provide insight into the methods and simulations used to aid in the design process of the devices investigated in this work.

## 2.1 The Finite Element Method and HFSS

FEM has many different applications to many different fields in engineering, not just electromagnetics. It is especially common to use it in complex physical systems involving partial differential equations that cannot be solved analytically like Maxwell's equations. The formulation of FEM consists of dividing a structure into smaller sections of finite dimensions called elements. The elements are connected via nodes. Each unique element is then solved independently of the others which greatly reduces the complexity for solving a physical system. A final solution is computed by assembling the individual elements and combining their solutions.

We used Ansys High Frequency Structure Simulator (HFSS; Canonsburg, PA; v. 15.0) to simulate the devices in this work. HFSS uses FEM to solve for the complex structure. It starts by dividing a geometric model into many different tetrahedral elements. The components of the field tangential to three edges meeting a vertex of the tetrahedron are stored at the vertex itself. The vector field, which is also tangential to a face and normal to an edge, is stored at the midpoint of the tetrahedron edge. These stored values are then used to estimate the vector field quantity of the H-field and the E-field inside each tetrahedron. The estimation is done by an interpolation of a tangential element basis function the order of which can be selected by the user in the analysis options. The field quantities are then used to formulate Maxwell's equations and then

transformed into matrix equations that are solved through the program by using matrix solution techniques.

## 2.2 Scattering Parameters

The results we are interested in are the transmission, reflection, and the phase shift through the metasurfaces. There are some considerations that must be made with HFSS and antenna theory in general. The first thing to note is that in the 3D CAD environment of HFSS, any open unbound space is a perfect electric conductor. For our purposes, we want to create a two-port network out of an air- or vacuum-filled waveguide with our device in the middle of the waveguide.

At high frequencies voltage, current, impedance, and admittance become a rather abstract concept. A representation more in unity with direct measurements, and with the ideas of incident, reflected, and transmitted electromagnetic waves, is given by a mathematical tool called the scattering matrix. In a circuit context, the scattering matrix relates voltage incident on the ports to those reflected from the ports [19].

$$\begin{bmatrix} V_1^- \\ V_2^- \\ \vdots \\ V_N^- \end{bmatrix} = \begin{bmatrix} S_{11} & S_{12} & \cdots & S_{1N} \\ S_{21} & S_{22} & \ddots & \vdots \\ \vdots & \vdots & \ddots & \vdots \\ S_{N1} & S_{N2} & \dots & S_{NN} \end{bmatrix} \begin{bmatrix} V_1^+ \\ V_2^+ \\ \vdots \\ V_N^+ \end{bmatrix} \tag{2.2}$$

Equation 2.2 defines the S-parameters where N is the number of ports in the network.

HFSS is capable of formulating the electromagnetic scattering parameters of two-port systems with multiple modes. This is important for our purposes because observing anomalous reflection and transmission requires analyzing cross-polarized modes [8]. HFSS is also capable of analyzing the phase shift of the scattering parameters which is

critical for investigating the individual V-antenna elements of the unit cell.

The criteria for our designs to be successfully optimized are that, at a desired frequency, they should produce maximum magnitude for cross-polarized transmission and that each different V-antenna element is 45° different in terms of phase transmission from its neighbors in the unit cell sequence. This gives a full 360° phase gradient for the interface. The purpose of these simulations is to match results of previous works as in Ref. [8]. If HFSS is not successful in reproducing publish and tested results in the optical range, it is an unsuitable simulation environment and we would therefore need to try a different simulation environment or method with the device.

Figure 2.1 shows the analytically calculated results from Ref. [8]. The left picture shows the normalized amplitude of the cross-polarized scattered light of the V-antennas while the right picture shows the phase shift of each of the four V-antenna elements. The normalized amplitudes remain relatively uniform while the phase shifts between each antenna are clearly close to or exactly 45°. These consistent phase shifts between each

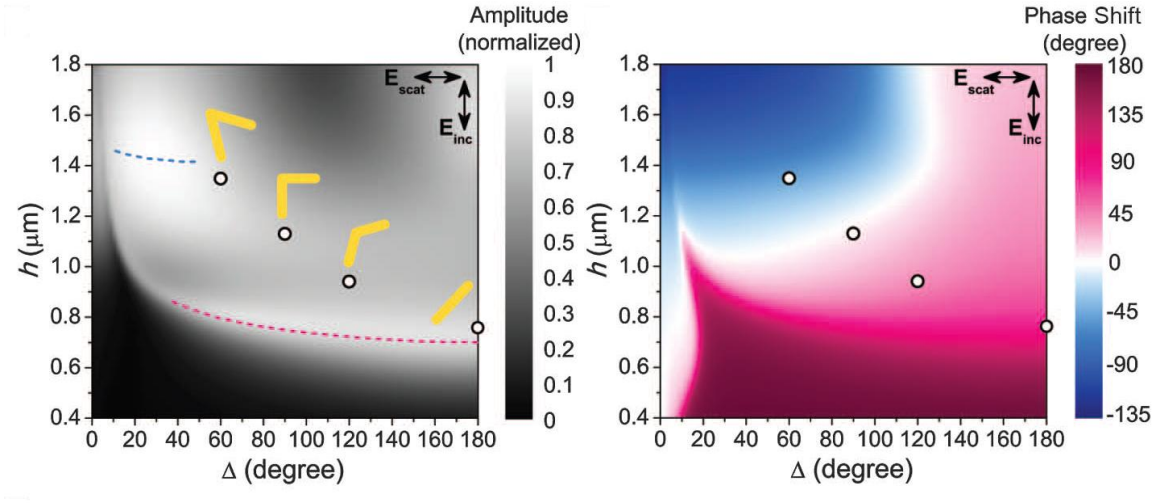


Figure 2.1 Results Expected at 8 μm. From [8]. Reprinted with permission from AAAS.

element means that the device can successfully steer an incoming beam of an electromagnetic wave of specific frequencies oblique to its surface. These results are also the same as the experimental results from Ref. [8] and are thus the results we need to match using the HFSS simulation environment.

One thing of note, however, is that the phase of a simulated or experimental device does not necessarily need to match exactly that of Figure 2.1 for each antenna as long as the phase difference between each antenna is close to or exactly at 45°. The normalized amplitude is an arbitrary value that designates the ratio of the transmission of the device with the gold nanorod antennas to that of the transmission with only silicon.

### 2.3 General Simulation Setup

Before testing the full phase gradient, it is important to test the individual unit cells of the individual V-antennas to check for the magnitudes of cross-polarized transmittance and phase shifts. These results will be used to test the accuracy of our simulation by comparing our results to those obtained in Ref. [8] and depicted in Figure 2.1. Geometry of one of the simulated V-antenna elements is shown in Figure 2.2. The arms are first created by using cylinder centered at the origin. A box with the arm length is attached at the center of the cylinder. Another cylinder is placed at the end of the arm with its center at the midpoint of the box-side. The arm is then replicated using the clone function in HFSS and then pivoted about the original cylinder-axis to create the final V-antenna.

Assigning the correct boundary conditions to define electromagnetic characteristics is critical. Ports are the only “boundary conditions” that define a surface

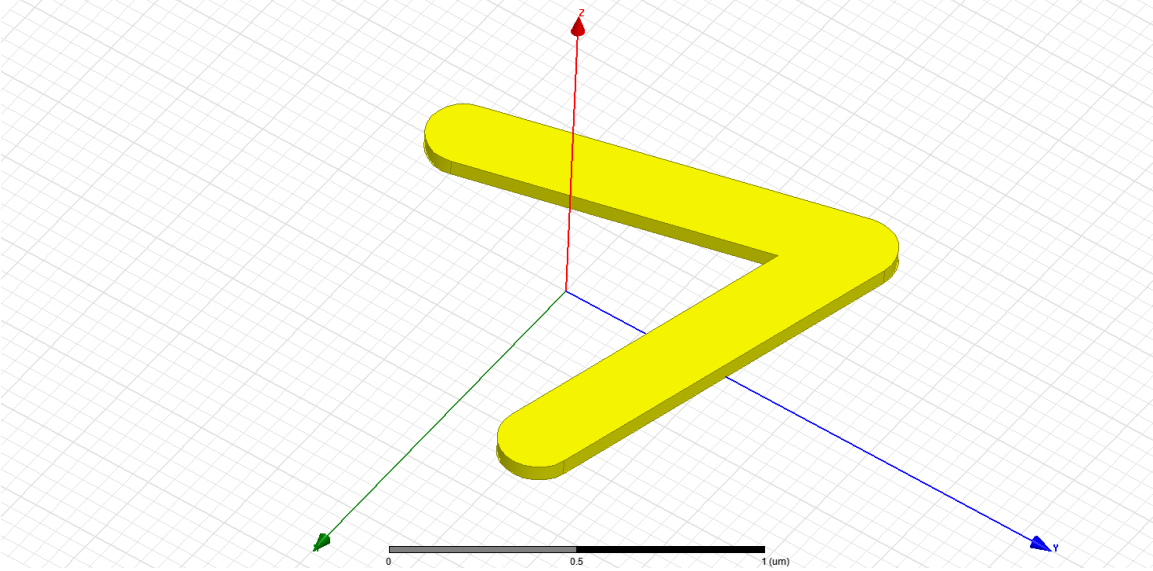


Figure 2.2 An Example of a V-antenna in the 3D CAD Environment for HFSS.

which permits energy to flow into and out of the structure so they will be used for measurements as discussed in the previous section.

Setting up an entire array of V-antenna unit cells to solve is tedious and requires more computation power than is available. In HFSS, it is possible to set up periodic boundary conditions for a single unit cell to approximate an infinitely large system. These are called the Master/Slave boundary conditions which allow for modelling infinite periodicity.

Figure 2.3 shows an example of the master/slave boundary conditions in HFSS. They force the E-field at each point on the slave boundary to match the E-field to within a phase difference on each corresponding point on the master boundary. The master/slave boundary conditions give linked boundaries for an infinite planar-periodic structure. However, there still needs to be at least one “open” boundary condition representing the boundary to infinite space above and below the air box. The Floquet port is a particular

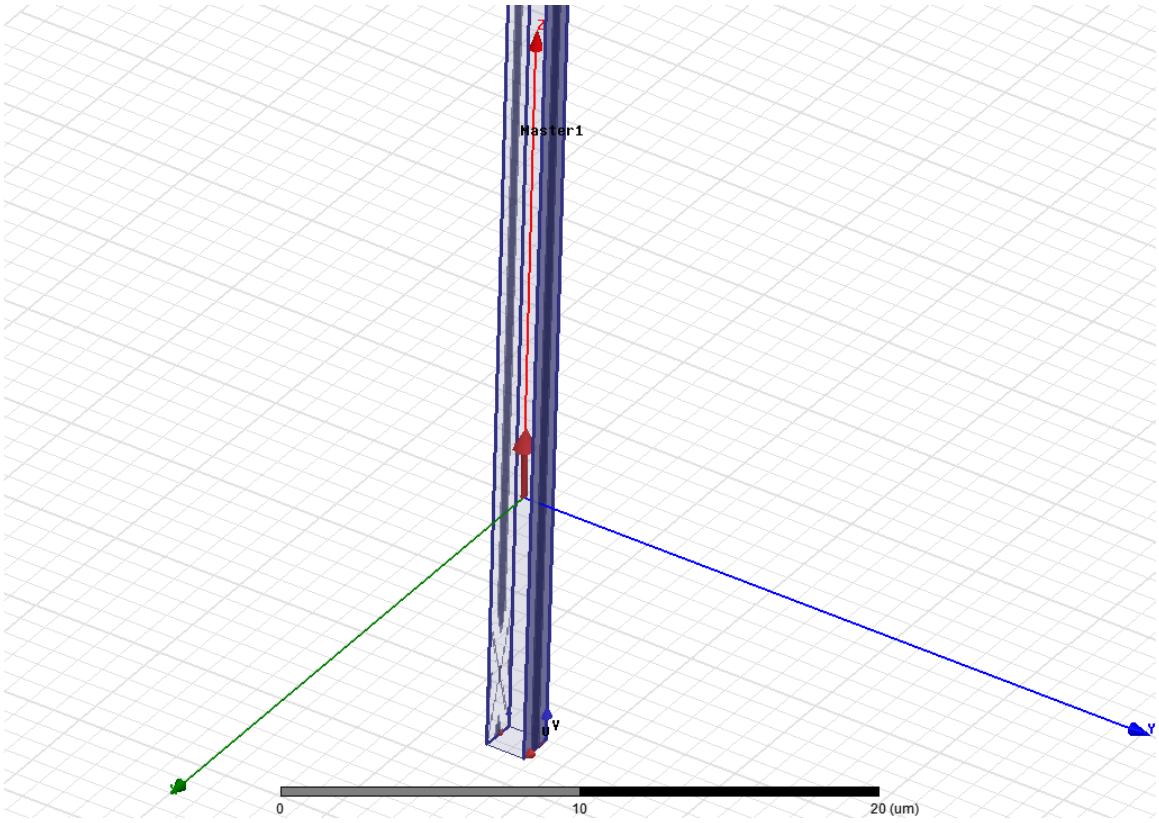


Figure 2.3 Example of Master/Slave Boundary Conditions in HFSS.

excitation that can be utilized to handle this exact case.

A Floquet port is closely related to a wave port in that a set of modes is used to represent the fields on the port boundary.

Fundamentally, the modes are plane waves with propagation direction set by the geometry frequency and geometry of the periodic structure. When a Floquet port is defined in HFSS, the program performs a modal decomposition that gives a scattering matrix connecting the Floquet modes. For these devices, we want two Floquet ports to excite the two spectral orthogonal modes $TM_{00}$ and $TE_{00}$ in order to measure both the co-polarization and cross-polarization magnitudes and phases. Figure 2.4 shows an example of a Floquet port used in our simulation environment.

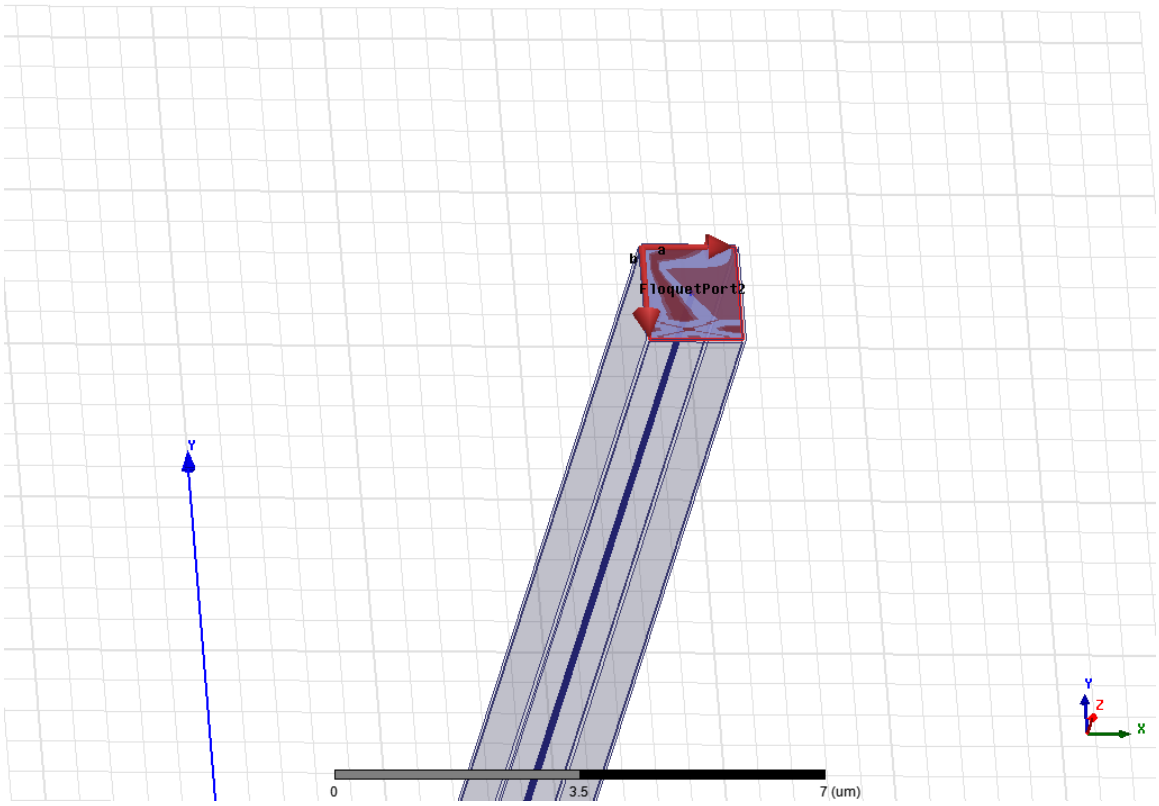


Figure 2.4 Example of a Floquet Port.

The vectors labeled '*a*' and '*b*' define the periodicity of the planar lattice; the direction of these vectors is important in defining the direction of the E-field for each mode. Vector '*a*' is along in the positive x direction while vector '*b*' is along the negative y direction. This ensures that the E-field in the $TE_{00}$ mode has a positive y polarity while giving to the E-field in the $TM_{00}$ mode a positive x polarity as defined by Floquet theory used in conjunction with the right hand rule thus keeping the modes consistent with the experiments and calculations performed in Ref. [8].

## 2.4 Simulated Results for Gold Nanorods on Silicon

Before even testing our own device design, it is absolutely necessary to replicate the results from previous papers [8]. The design in [8] utilizes gold with a depth of 50

nm. The antennas each have a width of 220 nm. The surface normal to the z axis for each element is 1.375 μm by 1.5 μm, which corresponds to a packing density of $\Gamma = 11$ μm.

The geometric parameters for the antenna arms are given in Table 2.1. What should be notable, given that the wavelength in which we are interested is 8 μm, is that these antennas are each less than $\frac{\lambda}{4}$ meaning that they should exhibit at least two resonant modes. This is the reason for utilizing V-antennas as opposed to an array of straight antennas: the double-resonant nature of the V-antennas means the device will be capable of achieving the required phase shifts while preserving large scattering amplitudes. A single antenna resonance would only be able to provide a range of phase of 180° between the scattered and incident light without resorting to mirror structures.

In order to properly simulate the device, we first define each element as a nanorod antenna which can be drawn as an amalgamation of three-dimensional z-normal cylinders and boxes. The final 3D CAD environment drawing of each V-antenna is shown from the top view in Figure 2.5. The gray blocks represent the silicon substrates which have bottom faces touching the Floquet port in order to simulate a semi-infinite structure. The

Table 2.1 Optical V-antenna Geometric Specifications

| **V Antenna Type** | **Arm length** |
|---|---|
| 60° | 1.35 μm |
| 90° | 1.13 μm |
| 120° | 0.94 μm |
| 180° | 0.75 μm |

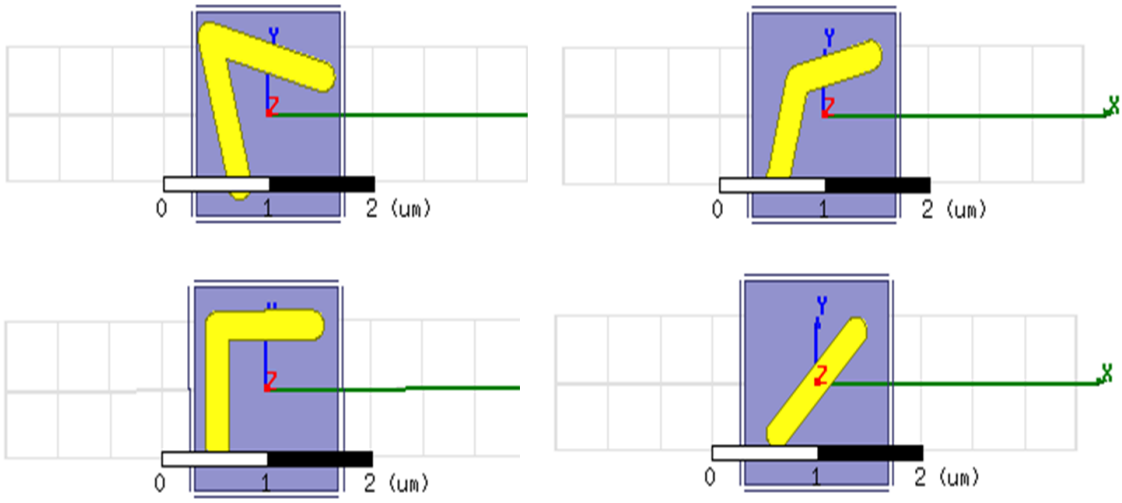


Figure 2.5 Optical V-antenna Designs for HFSS.

yellow shapes represent the nanorods themselves on top of the substrate facing at an angle of -45° along the xy plane and normal to the z-axis. The port at the ottom of the substrate touches the Floquet port on the negative side of the z-axis in order to model the substrate as being semi-infinite.

Each element was excited with Floquet ports from a wavelength of 6 µm (50 THz) to 18 µm (16.67 THz). The data for each element were then extracted from HFSS and plotted together in Matlab. Figure 2.6 shows the simulated cross-polarized transmission and phase of the antenna elements. It also shows the phase difference between neighboring antenna elements at the bottom. While at lower wavelengths (higher frequencies), the phase difference between each neighbor decreases while greatly increasing as the wavelength gets bigger (smaller frequencies).

Since Ref. [8] was tested at a wavelength of 8 µm, the transmittance, phase, and phase difference values at that point are what we are primarily analyzing. Table 2.2 gives the results of the transmission and phase for each V-antenna type.

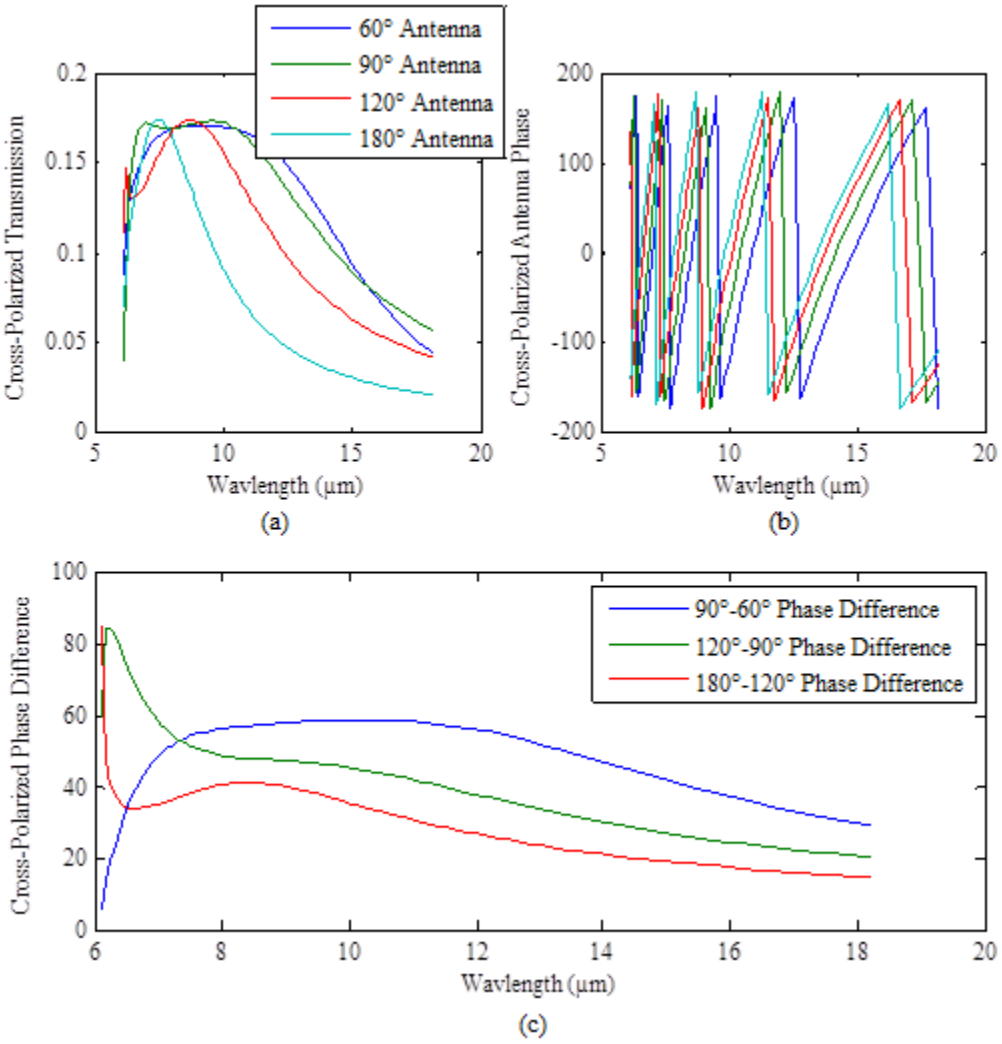


Figure 2.6 Analysis of Cross-polarized Transmission (a), Phase (b), and Phase Difference (c) of V-antenna Elements.

The results show good agreement with Ref. [8] with the phase differences for each neighboring element being ~40° and a consistent transmittance from each of the elements making it a suitable simulation environment for the devices.

After confirming an accurately modeled phase difference between the V-antenna elements at the frequencies of interest, we were able to do a full simulation of the anomalous refraction with the full unit cell.

An airbox is placed a quarter -wavelength away from the top of the structure. The

Table 2.2 Phase and Magnitude of Transmission for Optical Antennas at 8 µm

| **V-Antenna Type** | **Transmission** | **Φ** |
|---|---|---|
| 60° | 0.169 | -104.6° |
| 90° | 0.169 | -48.39° |
| 120° | 0.1669 | 0.2988° |
| 180° | 0.1655 | 40.77° |

electric field is then monitored along the surface of the airbox. Figure 2.7 shows anomalous refraction along with regular refraction (no angle) of the electric field at 8 µm. The magnitude of the electric field is related to its color in the image where red is the color with the highest magnitude while dark blue represents the lowest magnitude as shown in the legend. The angle between the anomalous refraction and the regular refraction is large enough that the electric fields are considered split and therefore

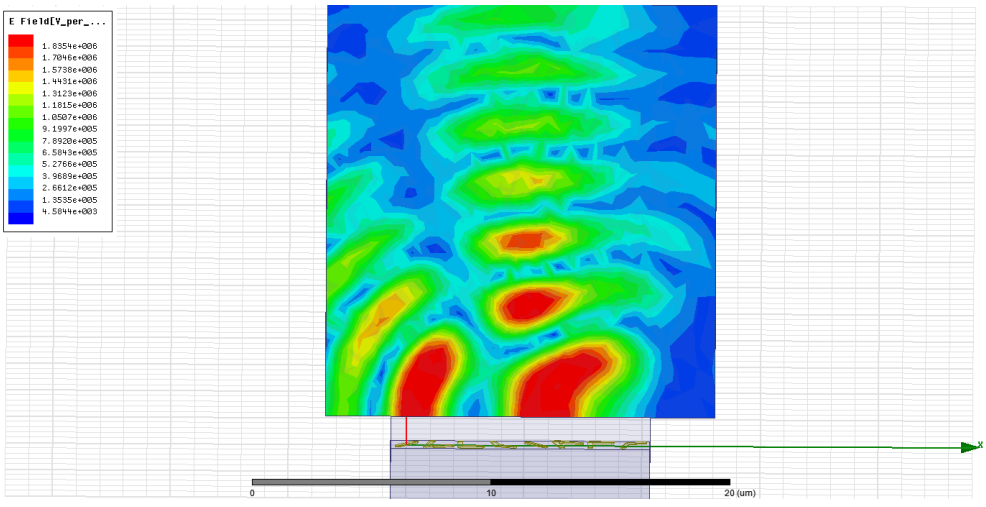


Figure 2.7 Anomalous Refraction and Regular Refraction Simulated in HFSS.

separate. By laws of conservation of energy a regular refraction will always exist in additional to an anomalous refraction no matter how consistent the phase difference between the antenna elements of the device.

# CHAPTER 3

## DEVICE FABRICATION AND EXPERIMENTS

The simulated structures showed the desired output in the simulation environment and correctly correlated with that of Ref. [8]. The next step is to change the material, size, and shape of the structures so that it can operate in the THz regime rather than the near-infrared regime. Given that the V-antennas worked well with HFSS in the optical regime, it should still be capable of simulating devices in the THz regime. The main difference is that we will have to model the substrate effects of the device rather than using a semi-infinite substrate. Given successful simulations, we can then move onto the real-world application stage and create a device using a MEMS-based printer as it is more efficient than fabricating the device using nanofabrication techniques.

This chapter seeks to cover how we simulated devices in the THz regime in order to have them exhibit phase gradient properties as those of the device in the optical regime from the previous chapter. The first section will introduce a gradual change from the first device in that it will be linearly scaled by wavelength to operate at the appropriate THz frequency. It will also introduce a change in the substrate material sapphire as that is the substrate that will be used for $VO_2$ deposition. The second section will introduce a second design scaled based on the geometric parameters attainable by an available MEMS-based

3D printer, as well as using silver for the material of the antennas and polyethylene terephthalate for the substrate as the printer will contain silver ink for printing the antenna devices and PET is a cheap, widely-available dielectric with properties suitable for the THz range. Finally, this chapter will conclude with the printing and time-domain spectroscopic results of the silver microrod devices on the PET substrates, both of which were performed by Andrew Paulsen of Dr. Nahata's research group. The experimental data will then be compared to that of the simulated data to show the accuracy of the simulations.

### 3.1 Simulated Results for Gold Microrods on Sapphire Scaled for THz

Since according to Ref. [8] the device can be scaled linearly, we started by scaling based on wavelength and chose 500 GHz (600 μm) as the frequency to which we wanted the device to scale. We first scale the device parameters by 75 times as that is the wavelength ratio for 8 μm and 500 GHz (600 μm). The antenna width is now 16.5 μm and the depth is now 100 nm. Table 3.1 shows the parameters for the antenna arm lengths for optimal output at 500 GHz.

Table 3.1 THz V-antenna Geometric Specifications

| **V-Antenna Type** | **Arm length** |
|---|---|
| 60° | 101.18 μm |
| 90° | 84.17 μm |
| 120° | 73 μm |
| 180° | 63.91 μm |

The THz V-antennas will not just be scaled up since the device is no longer in optical regions of frequency. Unlike with the optical V-antennas, the THz antennas must have their substrate modeled finitely as opposed to semi-infinitely.

Figure 3.1 shows an example of a V-antenna element modeled in an airbox with a finite substrate of 500 µm. The size of the airbox was made to be 6 mm in height, 106 µm in width (x axis), and 112.42 µm in length (y axis). These models were made and measured using the same method as before of using a parametric sweep on the geometry to determine the optimal geometry for the optimal transmission. After modeling and testing each system from 50 GHz to 550 GHz (6 mm to 546 µm) the results were extracted and plotted in Matlab.

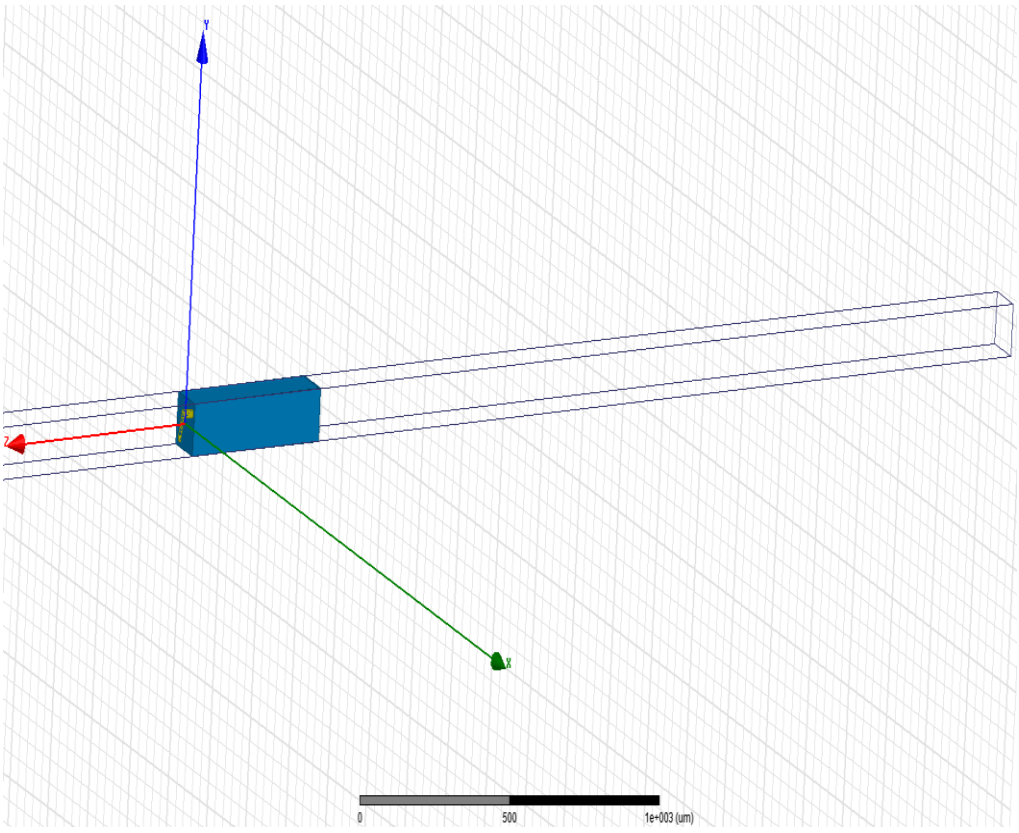


Figure 3.1 THz V-antenna with Finite Sapphire Substrate.

Figure 3.2 shows the plotted transmission amplitude, phase shift, and phase difference between neighboring antennas. It is noticeably different from Figure 2.6 which makes sense due to the increase in size and the change in the substrate material. Table 3.2 shows the phase and magnitude of the cross-polarized transmission at 500 GHz. The transmission is shown to be still in the same range.

With these parameters, we then create a new design for the unit cell, as seen in

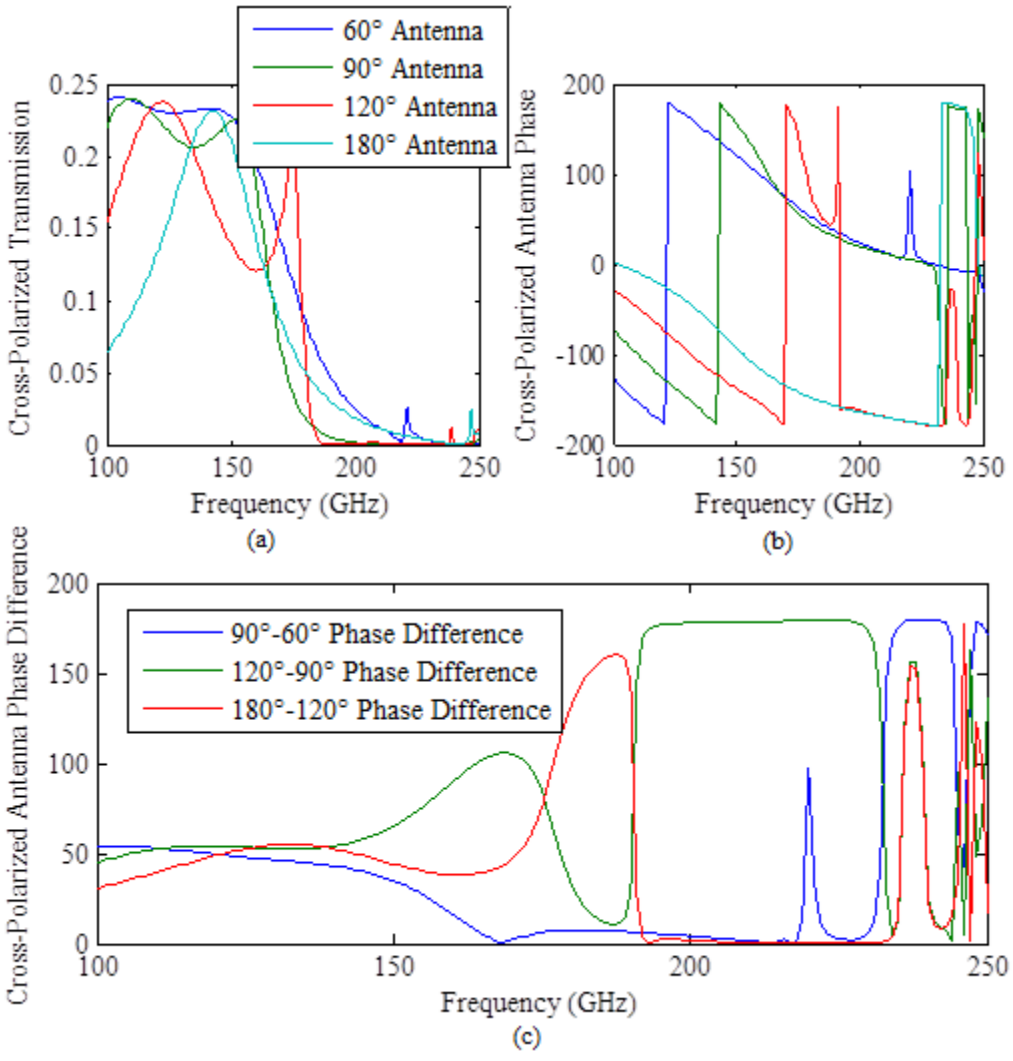


Figure 3.2 Analysis of Cross-polarized Transmission (a), Phase (b), and Phase Differences (c) of the Four THz Antenna Elements.

Table 3.2 Phase and Magnitude of Transmitted Cross-polarized EM Wave at 500 GHz

| **V-Antenna Type** | **Transmission** | **Φ** |
|---|---|---|
| 60° | 0.195 | 134.61° |
| 90° | 0.179 | -179.26° |
| 120° | 0.19 | -131.18° |
| 180° | 0.18 | -93.152° |

Figure 3.3. Since it is scaled linearly, the total period is now $\Gamma = 825$ µm. The vertical periodicity (for the y-direction) is 112.42 µm. Having drawn the full unit cell, including the boundary conditions as the method before, the full device is simulated at the optimum frequency and the electric field is plotted along the surface. The full unit cell simulated is shown in Figure 3.4. This cell is constructed in the same manner as Figure 2.7 with the geometry scaled up.

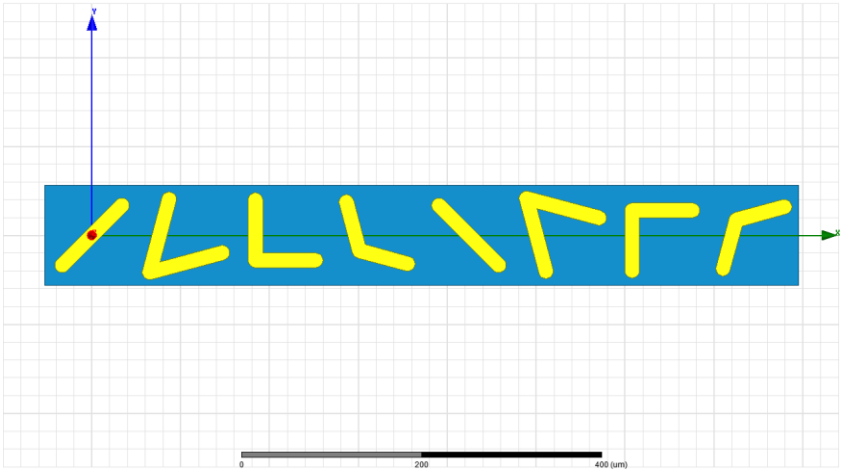

Figure 3.3 Individual THz V-antenna Elements on Unit Cell.

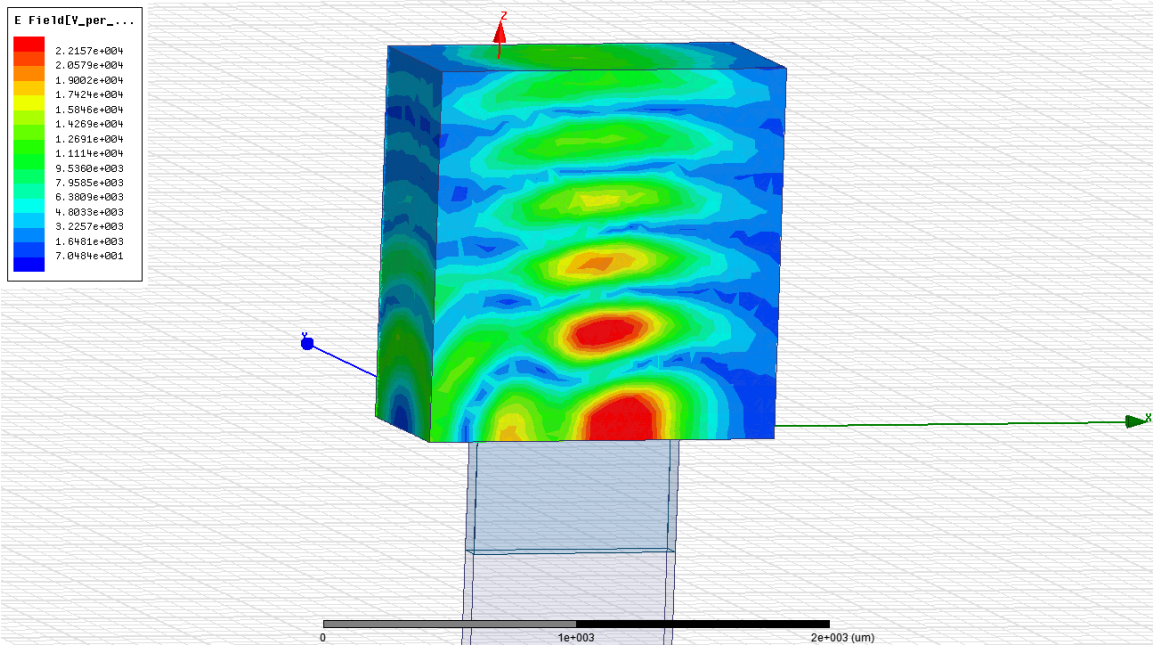


Figure 3.4 Anomalous Refraction and Regular Refraction of THz Device at 500 GHz.

As expected, the anomalous refraction is much weaker in comparison to that in Figure 2.7. One possible reason the beam steering is much less efficient is due to the effect of the finite substrate thickness. Despite this, it is still fully capable of steering an electromagnetic beam as shown in the figure. However, the anomalously refracted beam is very clearly low in terms of intensity in comparison to the optical device transmission.

### 3.2 Simulated results for silver microrods on PET

The final simulation set was done for silver microrod antennas on a polyethylene terephthalate (PET) substrate. The reason for using this particular setup as a preliminary device is due to the ease of printing this design with a printer as stated above. One other advantage in addition to easy fabrication is that PET is transparent for THz radiation and has a low absorption coefficient in the THz frequency range [22] [27] [28].

Table 3.3 shows the parameters of the device which are not optimized for any particular frequency and were rather chosen based on what would be easiest for the 3D MEMS printer. The widths are 150 µm for all but the 60° antenna which has a width of 170 µm. The antennas all have a depth of 1 µm with the substrate having a depth of 150 µm.

The most noticible difference between this device and the previous devices is how thin the substrate is. The airbox was made to be 1.96 mm in height and 1 mm in both width (x axis) and length (y axis). The Floquet ports are on the top and bottom faces of the air box normal to the z axis as before. The device Floquet ports were then excited using a frequency sweep from 50 GHz to 600 GHz.

Figure 3.5 shows an example of the silver antennas on the PET substrates as defined in HFSS. The antennas are created using similar methods from the previous sections with different materials such as PET for the substrate and silver for the antenna material.

Table 3.3 PET V-antenna Geometric Specifications

| **V-Antenna Type** | **Arm length** |
|---|---|
| 60° | 720 µm |
| 90° | 625 µm |
| 120° | 530 µm |
| 180° | 435 µm |

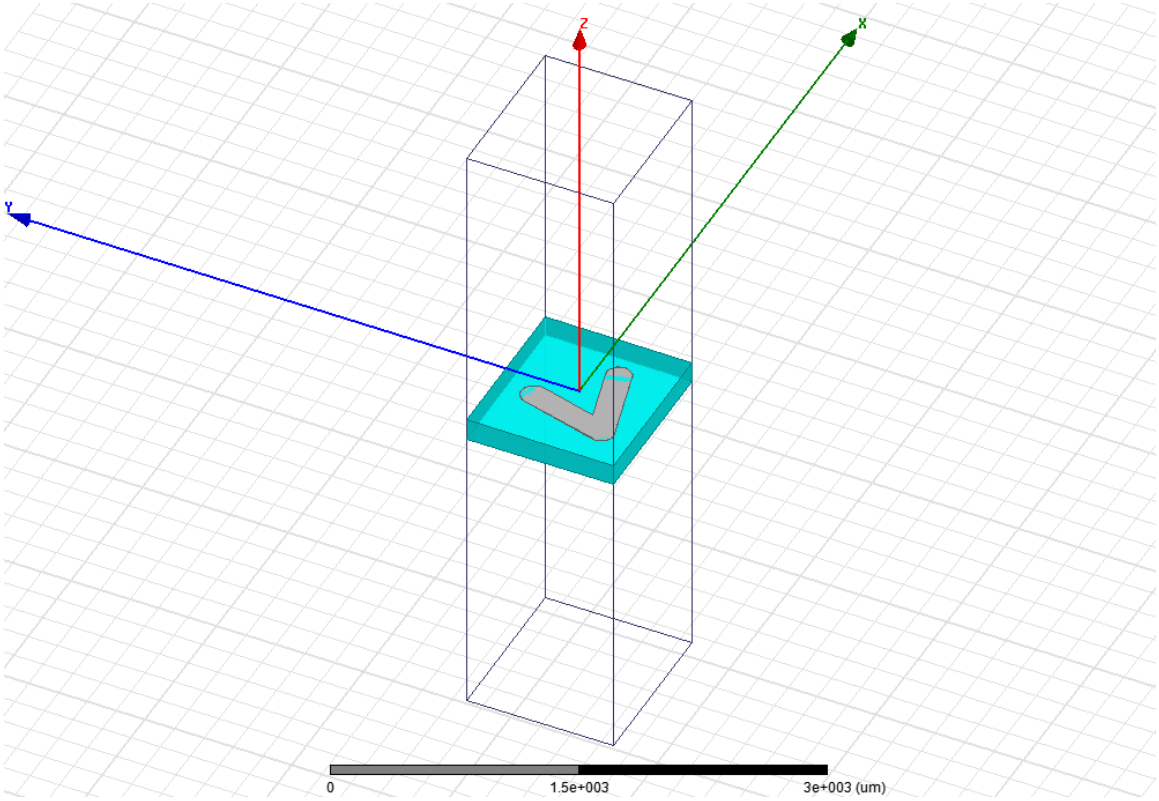


Figure 3.5 Example of a PET Antenna Device.

Figure 3.6 shows the cross-polarized transmission magnitude, phase, and phase difference between the four PET devices. What should be immediately noticeable is that resonances occur at frequencies below 300 GHz but are still considered to be in the millimeter range. Since the frequency is decreasing, the wavelength is also increasing allowing for less unstable results than in the optical range as shown in Figure 2.6. Figure 3.6 is plotted with frequency as the independent variable rather than wavelength. Table 3.4 gives the cross-polarized transmission and phase of the silver V-antennas on the PET substrates at 143 GHz as that is the frequency with the closest results to those desired, though it is in the microwave range as opposed to the THz range. While the phase

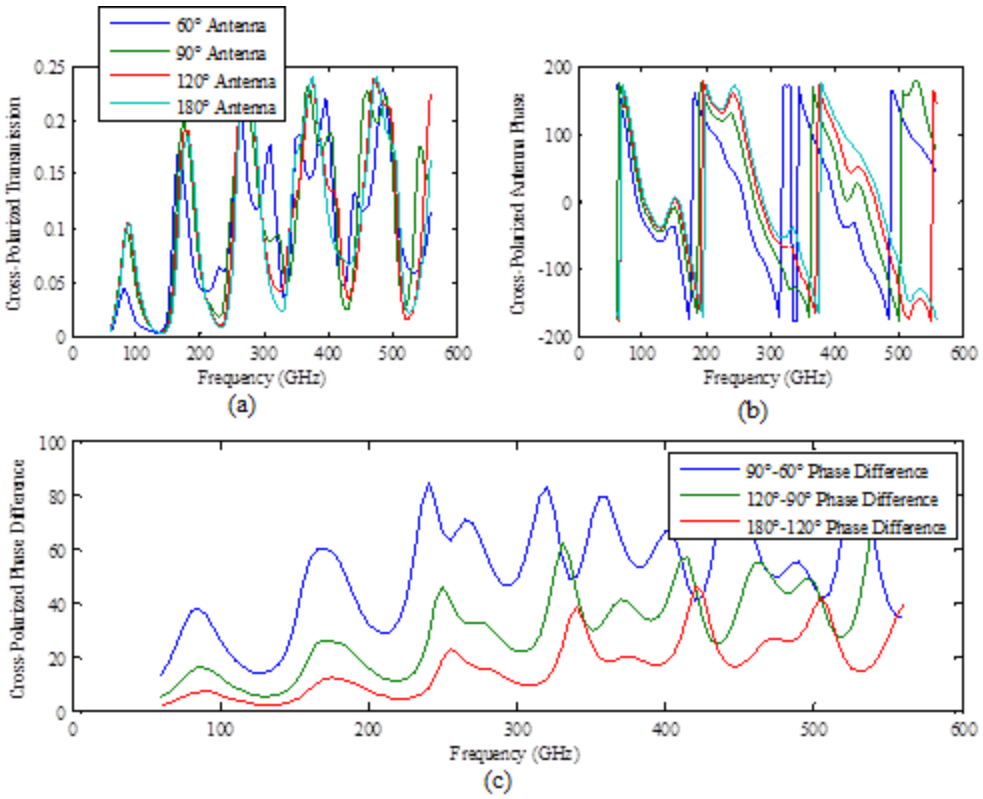


Figure 3.6 Analysis of Cross-polarized Transmission (a), Phase (b), and Phase Changes (c) of Four Silver Antenna Elements on PET Substrate.

differences between neighboring antennas are not all 45°, the average of the differences between each is 45° meaning it is still theoretically possible for the device to steer beams albeit inefficiently. While three of the antennas are in range with each other for transmission, the 120° antenna stands out as having greater than 20% transmission. Despite the minimum amount of optimization put into the process of creating this device, its results show consistent optimal phase differences.

Table 3.4 Phase and Magnitude of Transmitted Cross-polarized EM Wave at 118 GHz

| **V-Antenna Type** | **Transmission** | **Φ** |
|---|---|---|
| 60° | 0.228 | -168.3° |
| 90° | 0.23 | -122.7° |
| 120° | 0.234 | -78.47° |
| 180° | 0.23 | -34.87° |

### 3.3 Silver Microrod Antennas on PET Fabrication

An Epson Workforce 30 color inkjet printer with conductive silver ink was used to print V-antenna arrays of each individual V-antenna element on sheets of PET. Figure 3.7 depicts a microscope image of an area of the printed device. The printing was done by Andrew Paulsen of Dr. Nahata's research group. The Epson Workforce 30 color inkjet printer and the lab were provided by Dr. Nahata.

### 3.4 Experimental Setup

The experiments were performed by Andrew Paulsen of Dr. Nahata's group research group. He used an amplified Ti:sapphire laser as the optical source for all the THz TDS measurements. The output of the laser was split 80:20 to yield the optical pump and probe beams, respectively. A broadband THz wave was generated using a 1 mm thick ZnTe crystal and a paraboloidal mirror was used to collect and collimate the THz radiation as it was propagated from the emitter to the sample, resulting in a beam that was


Figure 3.7 Microscope Images of Silver Antennas on PET.

normally incident onto the printed device. A second off-axis paraboloidal mirror was used to refocus the transmitted THz radiation onto a 1 mm thick ZnTe detection crystal, which allowed for coherent detection of the radiation via electro-optic sampling [24] [25] [26].

Figure 3.8 shows the general setup for time-domain spectroscopy. As mentioned above, the detector for their setup is a 1 mm thick ZnTe detection crystal. These tests were performed at room temperature (27 °C) to ensure stable testing conditions for the TDS experiment.

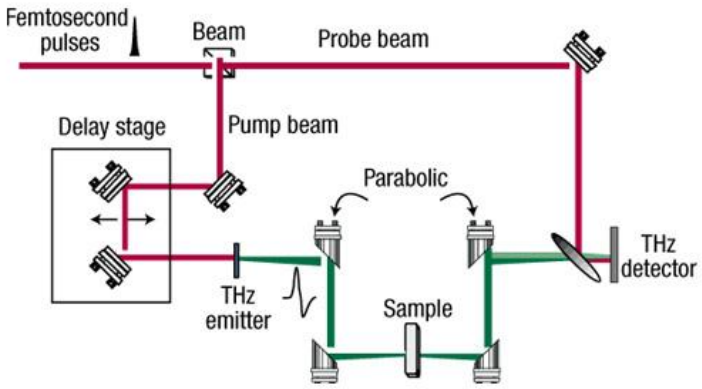


Figure 3.8 General TDS Setup. Reprinted by permission from MacMillan Publishers Ltd: Nature Materials [23], Copyright 2002.

### 3.5 Results

The results from the time-domain spectroscopy for each device were extracted from the TDS results and then plotted. The type of setup for our TDS is shown in Figure 3.8.

Figure 3.9 shows the plotted cross-polarized transmission and phase shift of the device given by the TDS. The results clearly show a 135° overall phase shift between the red and blue lines between 100 GHz and 200 GHz so it is in that range we used to find a specific frequency to analyze the output of the device.

Zooming in closely to the results shows the phase shift at which the antenna results are at or near 45° and have a relatively consistent phase difference between each element at about 118.5 GHz. This makes it at or close to the optimum frequency to measure the phase shifts and the transmissions for the experimental results.

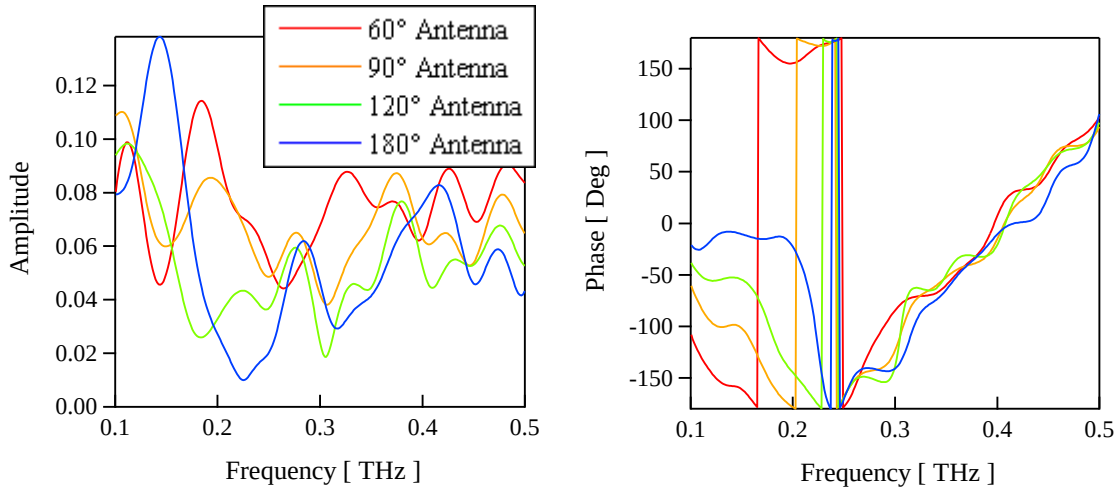


(a) (b)

Figure 3.9 TDS Measured Amplitude (a) and Phase (b) with PET Substrate Device.

Table 3.5 compares the simulated results to that of the experimental results at the frequency of interest which is 118.5 GHz for the experimental results and 118 GHz for the simulated results as that is the closest match in phase shift to that of the experimental results. The simulated transmission is obviously higher for the simulated environment as a simulation environment assumes perfect conditions. Other than a vastly different transmittance, which might be owed to fabrication imperfections, lower effective conductivity, sample roughness, sample alignment etc., both results between each neighbor very close to or exactly at 45°. This means the HFSS simulation has good qualitative accuracy in replicating real experimental results for TDS with a lower transmitted power.

Table 3.5 Comparison of Experimental and Simulated Results of PET Antennas at 118 GHz

| **V-Antenna Type** | **Simulated Transmission** | **Experimental Transmission** | **Simulated Phase Shift** | **Experimental Phase Shift** |
|---|---|---|---|---|
| 60° | 0.228 | 0.09 | -152.5° | -142.7° |
| 90° | 0.23 | 0.09 | -118.2° | -106.2° |
| 120° | 0.234 | 0.09 | -62.64° | -63.56° |
| 180° | 0.23 | 0.09 | -17.42° | -17.958° |

# CHAPTER 4

# CONCLUSION

We performed detailed investigations into the design, simulation, and fabrication of antenna array devices in the THz region and replicated previous results through simulations; we also performed experimental investigations with devices fabricated through means of a MEMS-based printer. The results from the experiment correlated strongly with the results from the simulation. The device was also discussed to be capable of steering beams in the THz regime in both the experimental and simulation environment.

To conclude, we used the extracted properties of our $VO_2$ sample to simulate a full unit cell of our proposed device in the THz regime. The dimensions of the antennas and device were the same as those from section 3.1 with the main difference being a sapphire substrate as opposed to PET. The simulated device was capable of steering beams at a ~35° angle at 600 GHz in the metallic state and keep the beam straight when in the insulated state at the same frequency.

Figure 4.1 shows the full unit cell simulation of the $VO_2$ structure in an insulated state. The beam flows through straight ahead as expected as it is not being affected by the $VO_2$. It is safe to say that the simulated $VO_2$ acts as an insulator that allows the beam to pass straight through the device with no deviation in its path.

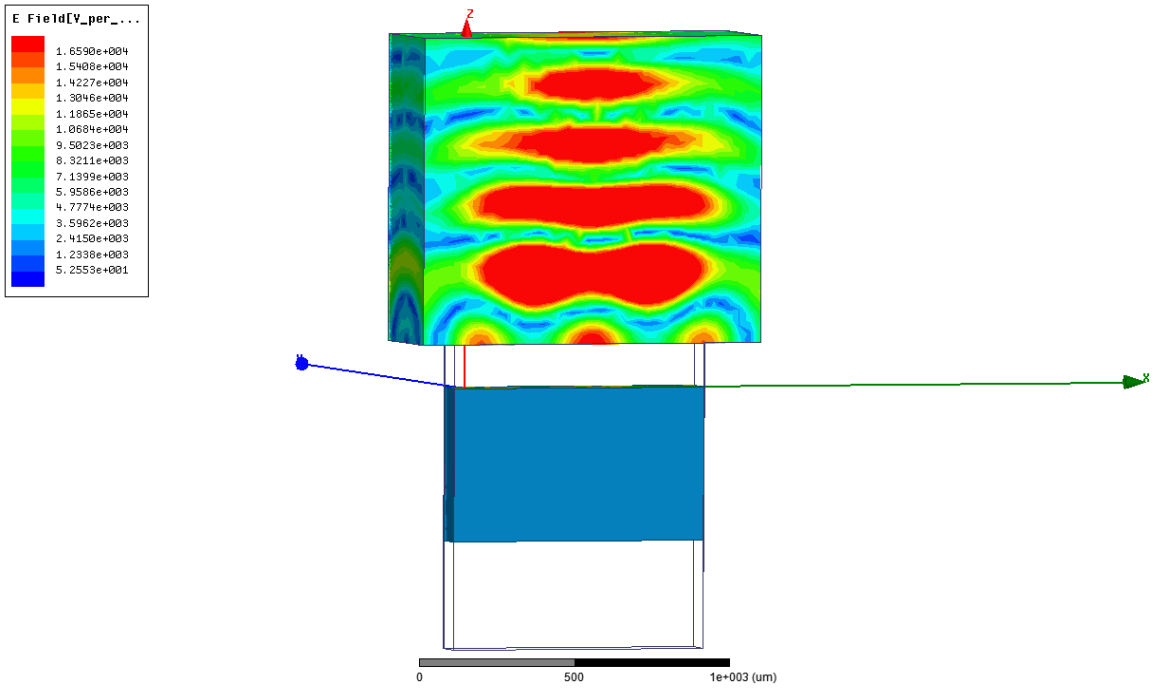


Figure 4.1 Simulation of $VO_2$ in Insulated State at 600 GHz.

Figure 4.2 shows a simulation of the device in the metallic state. The anomalous refraction is very much present in this simulation and steers to an estimated angle of ~35°. Compare to Figure 4.1 which has the exact same frequency parameters but different conductivity for the material and it is clear the simulation correctly demonstrates that the $VO_2$ heated to the proper temperature will produce beams-steering.

Based upon our previous results in the previous sections, both experimentally and in simulation, it is safe to say that our simulation produces the desired result of the unheated and heated $VO_2$ device. It is after this process which we would be able to begin the construction of our dynamic beam-steering antenna used to function as close to an omnidirectional antenna in the THz range as possible without losing as much gain as a proper omnidirectional antenna in the THz range would require.

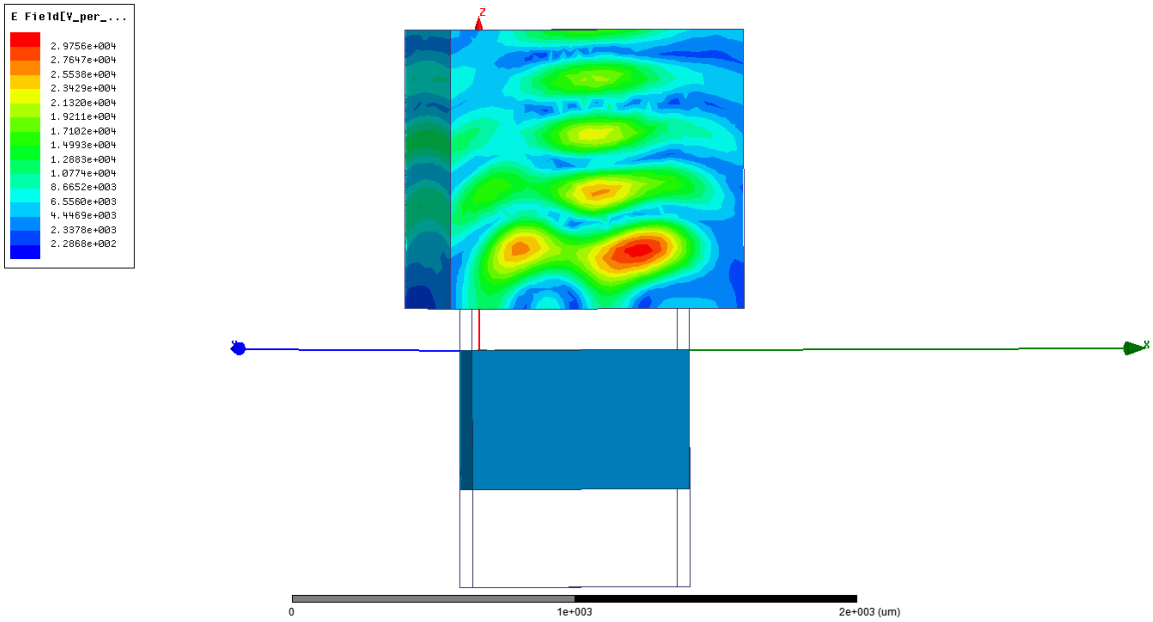


Figure 4.2 Simulation of $VO_2$ in Metallic State at 600 GHz.

### 4.1 Future Work

The results from the simulated structures show very good promise for a $VO_2$-based device. Now that we have shown that beam steering is possible with a preliminary device in the THz range in both experimental and simulation environments, the next course of action would be to use $VO_2$ as the material for the antenna devices. It is now simply a matter of optimizing the geometric structure of the device to give the device a full design with the full 360° phase shift. Then printing the device through the use of a MEMS printer or fabricating it with photolithography. The device would then be tested for its beam-steering capabilities using a similar setup to that of Figure 1.8.

## REFERENCES


[1] J. B. Pendry, D. Schurig, and D. R. Smith, "Controlling electromagnetic fields," *Science*, vol. 312, no. 5781, pp. 1780–1782, Jun. 2006.

[2] V. G. Veselago, "The electrodynamics of substances with simultaneously negative values of ε and μ," *Soviet Physics Uspekhi*, vol. 10, no. 4, pp. 509–514, Apr. 1968.

[3] C. Huygens and M. Blay, *Traité de la lumière*. Paris: Dunod, 1992.

[4] N. Yu and F. Capasso, "Flat optics with designer metasurfaces," *Nat Mater*, vol. 13, no. l.2, pp. 139-150, Feb. 2014.

[5] R. P. Feynman and A. R. Hibbs, *Quantum mechanics and path integrals*. New York: McGraw-Hill, 1965.

[6] S. D. Brorson and H. A. Haus, "Diffraction gratings and geometrical optics," *Journal of the Optical Society of America B*, vol. 5, no. 2, p. 247, Feb. 1988.

[7] R. P. Feynman, A. R. Hibbs, and D. F. Styer, *Quantum mechanics and path integrals*, Emended ed. Mineola, N.Y: Dover Publications, 2010.

[8] N. Yu, P. Genevet, M.A. Kats, F. Aieta, J.-P. Tetienne, F. Capasso, and Z. Gaburro, "Light propagation with phase discontinuities: generalized laws of reflection and refraction," *Science*, vol. 334, no. 6054, pp. 333-337, Oct. 2011.

[9] Nanfang Yu, P. Genevet, F. Aieta, M. A. Kats, R. Blanchard, G. Aoust, J.-P. Tetienne, Z. Gaburro, and F. Capasso, "Flat optics: controlling wavefronts with optical antenna metasurfaces," *IEEE Journal of Selected Topics in Quantum Electronics*, vol. 19, no. 3, pp. 4700423–4700423, May 2013.

[10] G. P. Williams, "Filling the THz gap—high power sources and applications," *Reports on Progress in Physics*, vol. 69, no. 2, pp. 301–326, Feb. 2006. doi:10.1088/0034-4885/69/2/R01

[11] A. Blain, "Submillimeter galaxies," *Physics Reports*, vol. 369, no. 2, pp. 111–176, Oct. 2002.

[12] J. Wei, D. Olaya, B. S. Karasik, S. V. Pereverzev, A. V. Sergeev, and M. E. Gershenson, "Ultrasensitive hot-electron nanobolometers for terahertz astrophysics," *Nature Nanotechnology*, vol. 3, no. 8, pp. 496–500, Aug. 2008.

[13] N. F. Mott, *Metal-insulator transitions*, 2nd ed. London ; New York: Taylor & Francis, 1990.

[14] N. F. Mott and L. Friedman, "Metal-insulator transitions in $VO_2$, $Ti_2O_3$ and $Ti_{2-x}V_xO_3$," *Philosophical Magazine*, vol. 30, no. 2, pp. 389–402, Aug. 1974.

[15] A. Zylbersztejn, "Metal-insulator transition in vanadium dioxide," *Physical Review B*, vol. 11, no. 11, pp. 4383–4395, Jun. 1975.

[16] C. Berglund and H. Guggenheim, "Electronic properties of $VO_2$ near the semiconductor-metal transition," *Physical Review*, vol. 185, no. 3, pp. 1022–1033, Sep. 1969.

[17] J. C. Maxwell, "A dynamical theory of the electromagnetic field," *Philosophical Transactions of the Royal Society of London*, vol. 155, no. 0, pp. 459–512, Jan. 1865.

[18] X. Lü, W. Yang, Z. Quan, T. Lin, L. Bai, L. Wang, F. Huang, and Y. Zhao, "Enhanced electron transport in Nb-doped $TiO_2$ nanoparticles via pressure-induced phase transitions," *Journal of the American Chemical Society*, vol. 136, no. 1, pp. 419–426, Jan. 2014.

[19] D. M. Pozar, *Microwave engineering*, 4th ed. Hoboken, NJ: Wiley, 2012.

[20] Y.-S. Lee, *Principles of terahertz science and technology*, 1st ed. New York, NY: Springer, 2008.

[21] P. H. Siegel, "THz instruments for space," *IEEE Transactions on Antennas and Propagation*, vol. 55, no. 11, pp. 2957–2965, Nov. 2007.

[22] F. Miyamaru, S. Kuboda, K. Taima, K. Takano, M. Hangyo, and M. W. Takeda, "Three-dimensional bulk metamaterials operating in the terahertz range," *Applied Physics Letters*, vol. 96, no. 8, p. 081105, 2010.

[23] B. Ferguson and X.-C. Zhang, "Materials for terahertz science and technology," *Nature Materials*, vol. 1, no. 1, pp. 26–33, Sep. 2002.

[24] B. Gupta, S. Pandey, S. Guruswamy, and A. Nahata, "Terahertz plasmonic structures based on spatially varying conductivities," *Advanced Optical Materials*, vol. 2, no. 6, pp. 565–571, Jun. 2014.

[25] A. Paulsen and A. Nahata, "K-space design of terahertz plasmonic filters," *Optica*, vol. 2, no. 3, p. 214, Mar. 2015.

[26] A. Nahata, A. S. Weling, and T. F. Heinz, "A wideband coherent terahertz spectroscopy system using optical rectification and electro-optic sampling," *Applied Physics Letters*, vol. 69, no. 16, p. 2321, 1996.

[27] D. Grischkowsky, S. Keiding, M. van Exter, and C. Fattinger, "Far-infrared time-domain spectroscopy with terahertz beams of dielectrics and semiconductors," *Journal of the Optical Society of America B*, vol. 7, no. 10, p. 2006, Oct. 1990.

[28] Jin, Yun-Sik, Kim, Geun-Ju, and Jeon, Seok-Gy, "Terahertz dielectric properties of polymers." *Journal of the Korean Physical Society*, vol. 49, no. 2, p. 513-517, Aug. 2006.

[29] Z. Tao, T.-R. T. Han, S. D. Mahanti, P. M. Duxbury, F. Yuan, C.-Y. Ruan, K. Wang, and J. Wu, "Decoupling of structural and electronic phase transitions in $VO_2$," *Physical Review Letters*, vol. 109, no. 16, Oct. 2012.

[30] M. M. Qazilbash, M. Brehm, B.-G. Chae, P.-C. Ho, G. O. Andreev, B.-J. Kim, S. J. Yun, A. V. Balatsky, M. B. Maple, F. Keilmann, H.-T. Kim, and D. N. Basov, "Mott transition in $VO_2$ revealed by infrared spectroscopy and nano-imaging," *Science*, vol. 318, no. 5857, pp. 1750–1753, Dec. 2007.

[31] H. Yan, F. Xia, W. Zhu, M. Freitag, C. Dimitrakopoulos, A. A. Bol, G. Tulevski, and P. Avouris, "Infrared spectroscopy of wafer-scale graphene," *ACS Nano*, vol. 5, no. 12, pp. 9854–9860, Dec. 2011.

[32] R. Yan, B. Sensale-Rodriguez, L. Liu, D. Jena, and H. G. Xing, "A new class of electrically tunable metamaterial terahertz modulators," *Optics Express*, vol. 20, no. 27, p. 28664, Dec. 2012.

[33] B. Sensale-Rodriguez, R. Yan, L. Liu, D. Jena, and H. G. Xing, "Graphene for reconfigurable terahertz optoelectronics," *Proceedings of the IEEE*, vol. 101, no. 7, pp. 1705–1716, Jul. 2013.

[34] T. L. Cocker, L. V. Titova, S. Fourmaux, H.-C. Bandulet, D. Brassard, J.-C. Kieffer, M. A. El Khakani, and F. A. Hegmann, "Terahertz conductivity of the metal-insulator transition in a nanogranular $VO_2$ film," *Applied Physics Letters*, vol. 97, no. 22, p. 221905, 2010.

[35] D. J. Hilton, R. P. Prasankumar, S. Fourmaux, A. Cavalleri, D. Brassard, M. A. El Khakani, J. C. Kieffer, A. J. Taylor, and R. D. Averitt, "Enhanced photosusceptibility near $T_c$ for the light-induced insulator-to-metal phase transition in vanadium dioxide," *Physical Review Letters*, vol. 99, no. 22, Nov. 2007.

[36] C. Berglund and H. Guggenheim, “Electronic properties of $VO_2$ near the semiconductor-metal transition,” *Physical Review*, vol. 185, no. 3, p. 1022, 1969.

[37] M. Tinkham, “Energy gap interpretation of experiments on infrared transmission through superconducting films,” *Physical Review*, vol. 104, no. 3, pp. 845–846, Nov. 1956.

[38] A. Roggenbuck, H. Schmitz, A. Deninger, I. C. Mayorga, J. Hemberger, R. Güsten, and M. Grüninger, “Coherent broadband continuous-wave terahertz spectroscopy on solid-state samples,” *New Journal of Physics*, vol. 12, no. 4, p. 043017, Apr. 2010.